Molecular Cell

Article

Structural basis of the human transcriptional Mediator regulated by its dissociable kinase module

Graphical abstract

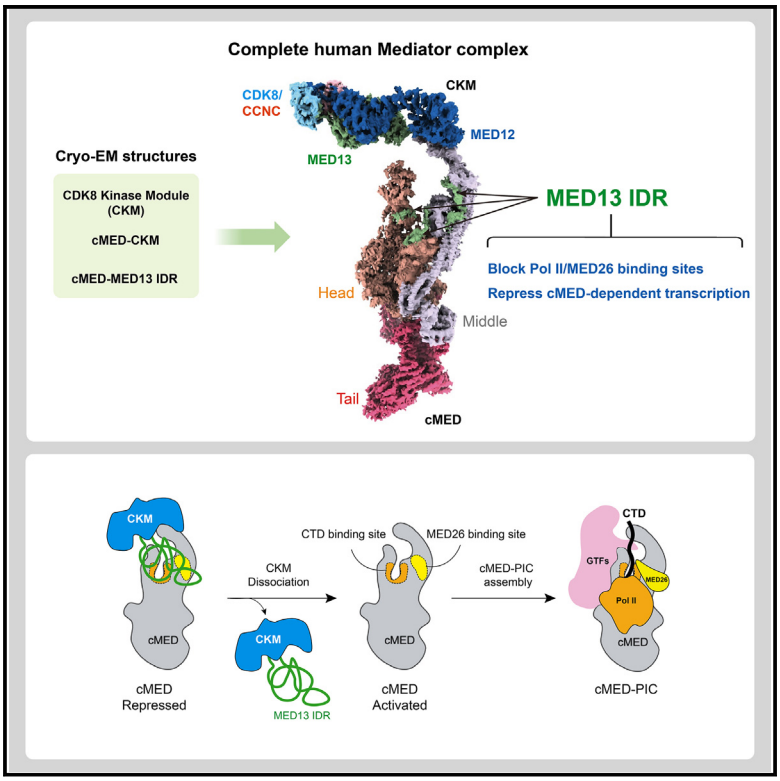

Highlights

- Structures of the complete human Mediator and its CDK8 kinase module (CKM) are presented
- CKM binds cMED through MED12 and the intrinsically disordered region (IDR) of MED13
- MED13 IDR blocks RNA Pol II/MED26 from binding to cMED by occupying their binding sites
- Human and yeast MED13 share a conserved mechanism for transcriptional repression

Authors

Ti-Chun Chao, Shin-Fu Chen, Hee Jong Kim, ..., Kenji Murakami, Thomas G. Boyer, Kuang-Lei Tsai

Correspondence

kenjim@pennmedicine.upenn.edu (K.M.), boyer@uthscsa.edu (T.G.B.), kuang-lei.tsai@uth.tmc.edu (K.-L.T.)

In brief

Chao and Chen et al. present cryo-EM structures of the complete human Mediator and its CDK8 kinase module (CKM). The CKM uses its MED13 IDR to occupy RNA-polymerase-II- and MED26-binding sites, blocking their interactions with Mediator and repressing Mediator-dependent transcription—a mechanism conserved in humans and yeast.

Chao et al., 2024, Molecular Cell *84*, 1–18
October 17, 2024
https://doi.org/10.1016/j.molcel.2024.09.001

CellPress

Molecular Cell

CellPress

Article

Structural basis of the human transcriptional Mediator regulated by its dissociable kinase module

Ti-Chun Chao,[1,8] Shin-Fu Chen,[1,8] Hee Jong Kim,[2] Hui-Chi Tang,[1] Hsiang-Ching Tseng,[1] An Xu,[4] Leon Palao III,[2] Subash Khadka,[3] Tao Li,[1] Mo-Fan Huang,[4,5] Dung-Fang Lee,[4,5,6,7] Kenji Murakami,[2,*] Thomas G. Boyer,[3,*] and Kuang-Lei Tsai[1,5,9,*]

[1]Department of Biochemistry and Molecular Biology, McGovern Medical School, University of Texas Health Science Center at Houston, Houston, TX, USA
[2]Department of Biochemistry and Biophysics, Perelman School of Medicine, University of Pennsylvania, Philadelphia, PA, USA
[3]Department of Molecular Medicine, University of Texas Health Science Center at San Antonio, San Antonio, TX, USA
[4]Department of Integrative Biology and Pharmacology, McGovern Medical School, University of Texas Health Science Center at Houston, Houston, TX, USA
[5]MD Anderson Cancer Center UTHealth Houston Graduate School of Biomedical Sciences, Houston, TX, USA
[6]Center for Precision Health, McWilliams School of Biomedical Informatics, The University of Texas Health Science Center at Houston, Houston, TX, USA
[7]Center for Stem Cell and Regenerative Medicine, The Brown Foundation Institute of Molecular Medicine for the Prevention of Human Diseases, The University of Texas Health Science Center at Houston, Houston, TX, USA
[8]These authors contributed equally
[9]Lead contact
*Correspondence: kenjim@pennmedicine.upenn.edu (K.M.), boyer@uthscsa.edu (T.G.B.), kuang-lei.tsai@uth.tmc.edu (K.-L.T.)
https://doi.org/10.1016/j.molcel.2024.09.001

SUMMARY

The eukaryotic transcriptional Mediator comprises a large core (cMED) and a dissociable CDK8 kinase module (CKM). cMED recruits RNA polymerase II (RNA Pol II) and promotes pre-initiation complex formation in a manner repressed by the CKM through mechanisms presently unknown. Herein, we report cryoelectron microscopy structures of the complete human Mediator and its CKM. The CKM binds to multiple regions on cMED through both MED12 and MED13, including a large intrinsically disordered region (IDR) in the latter. MED12 and MED13 together anchor the CKM to the cMED hook, positioning CDK8 downstream and proximal to the transcription start site. Notably, the MED13 IDR obstructs the recruitment of RNA Pol II/MED26 onto cMED by direct occlusion of their respective binding sites, leading to functional repression of cMED-dependent transcription. Combined with biochemical and functional analyses, these structures provide a conserved mechanistic framework to explain the basis for CKM-mediated repression of cMED function.

INTRODUCTION

The eukaryotic Mediator complex is a multisubunit (25–30 proteins), evolutionarily conserved transcriptional coactivator that transmits regulatory signals from activators and repressors to the RNA polymerase II (RNA Pol II) transcription machinery.[1–4] Given its large size, inherent kinase activity, and multiple subunit-specific protein interactions, Mediator is not only involved in the assembly of the preinitiation complex (PIC) at promoters during transcription initiation but also participates in regulating RNA Pol II pause and release prior to productive elongation.[5–7]

The Mediator complex is comprised of a large core (cMED), consisting of head, middle, and tail modules, as well as a dissociable CDK8 kinase module (CKM) (Figure 1A).[8–11] Functionally, cMED stimulates basal transcription by recruiting RNA Pol II to promoters, stabilizing PIC assembly, and stimulating phosphorylation of the RNA Pol II C-terminal domain (CTD).[3,12,13] In metazoans, cMED includes an additional subunit, MED26, which participates in recruiting either transcription factor II D (TFIID) or super elongation complex (SEC) to promoters for gene activation.[7,14] The CKM, comprising MED12, MED13, CCNC, and CDK8, can reversibly associate with cMED through its MED13 subunit.[9,15,16] In humans, MED12 directly interacts with and functionally stimulates the enzymatic activity of CDK8, a colorectal cancer oncoprotein.[17–19] In vertebrates, the CKM includes distinct paralogous subunit pairs (MED12/12L, MED13/13L, and CDK8/CDK19) that assemble with CCNC in

Please cite this article in press as: Chao et al., Structural basis of the human transcriptional Mediator regulated by its dissociable kinase module, Molecular Cell (2024), https://doi.org/10.1016/j.molcel.2024.09.001

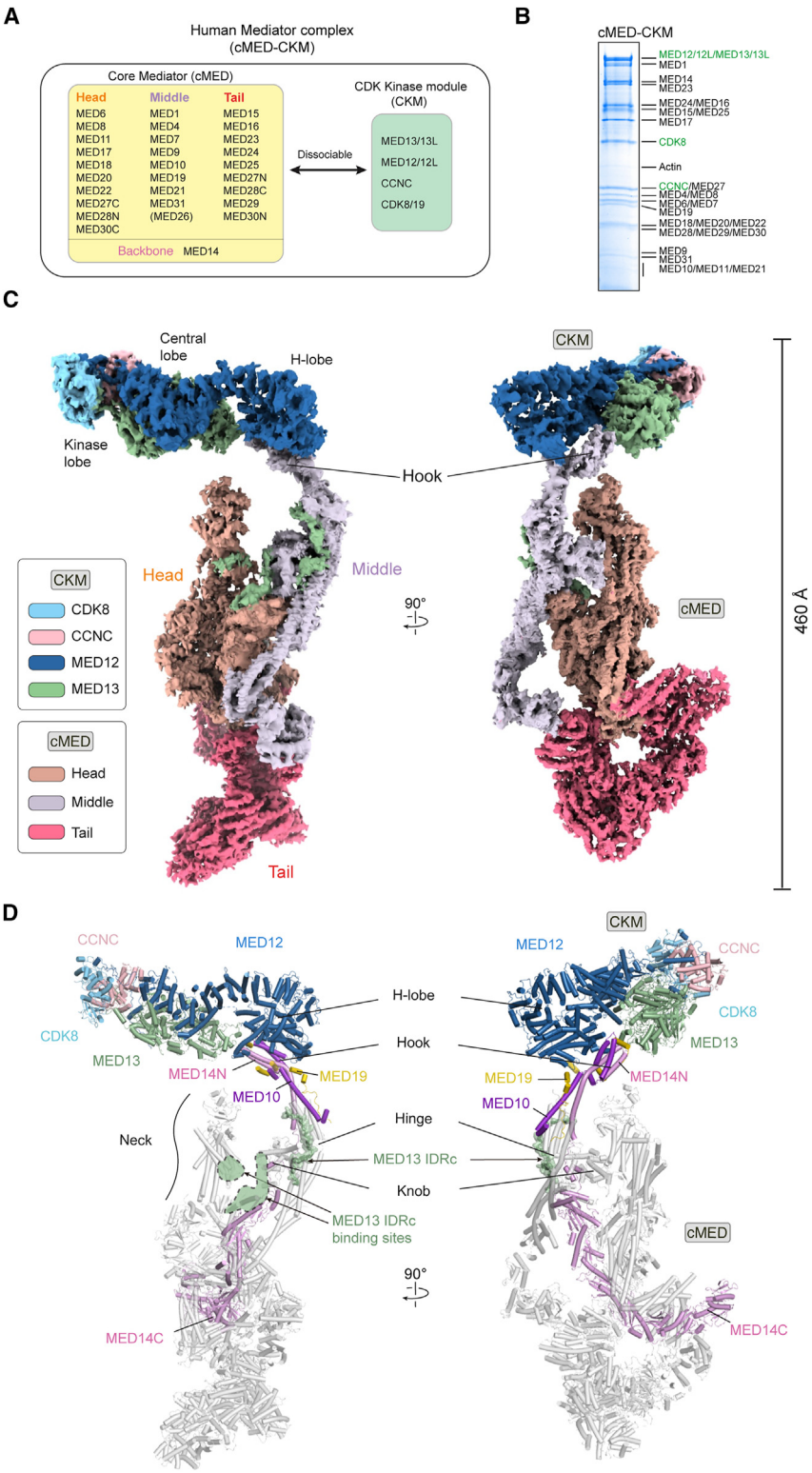

Figure 1. Structure of the complete human Mediator

(A) Subunit composition of cMED and CKM, with the Metazoan-specific subunit MED26 in parentheses.

(B) SDS-PAGE of purified Mediator.

(C) Composite cryo-EM map of human cMED-CKM. The average resolutions for cMED and CKM are 4.7 and 6.7 Å, respectively.

(D) Atomic model of human cMED-CKM, with MED13 IDR bound to the hinge of the middle module. Two additional MED13-IDR-binding sites on cMED are marked by green shapes.

repressor of transcription.[8,9,21] Recent studies, however, have shown that the CKM also plays a positive role in gene expression by participating in the regulation of RNA Pol II pausing and release during post-initiation events.[22–24]

Prior structural studies of cMED with the PIC have provided mechanistic details regarding their assembly process with an activator-promoter DNA complex to initiate transcription.[4,25–31] The structure of yeast CKM revealed its subunit organization, the mechanism of Med12-dependent Cdk8 activation, and the Argonaute (Ago)-like Med13 that includes a large intrinsically disordered region (IDR).[32] Despite these advances, high-resolution structural details of the complete human Mediator, comprising CKM bound to the cMED, remain unreported. Although low-resolution electron microscopy (EM) reconstructions of human and yeast cMED-CKM complexes exist,[8,9,15] the mechanism by which the CKM represses cMED-dependent transcription is still poorly understood.

Here, we present cryoelectron microscopy (cryo-EM) structures of the complete human Mediator complex, its free CKM, and cMED bound by the MED13 IDR at near-atomic resolution. Combined with biochemical and crosslinking mass spectrometry (XL-MS) analyses, this study provides a structural basis for the Mediator complex in a repressed state, elucidating the mechanism by which the CKM suppresses cMED-dependent transcription. We find that CKM binds to cMED through multiple interfaces involving the MED13 IDR and MED12 HEAT repeats. Notably, through its MED13 IDR, the CKM inhibits the binding of both RNA Pol II and MED26 to cMED. Functional analyses show that the MED13 IDR represses cMED-dependent transcription, a mechanism conserved among eukaryotes.

a mutually exclusive manner.[20] Based on its abilities to inhibit cMED-dependent transcription *in vitro* and preclude interaction of RNA Pol II with cMED, the CKM was initially considered a

Please cite this article in press as: Chao et al., Structural basis of the human transcriptional Mediator regulated by its dissociable kinase module, Molecular Cell (2024), https://doi.org/10.1016/j.molcel.2024.09.001

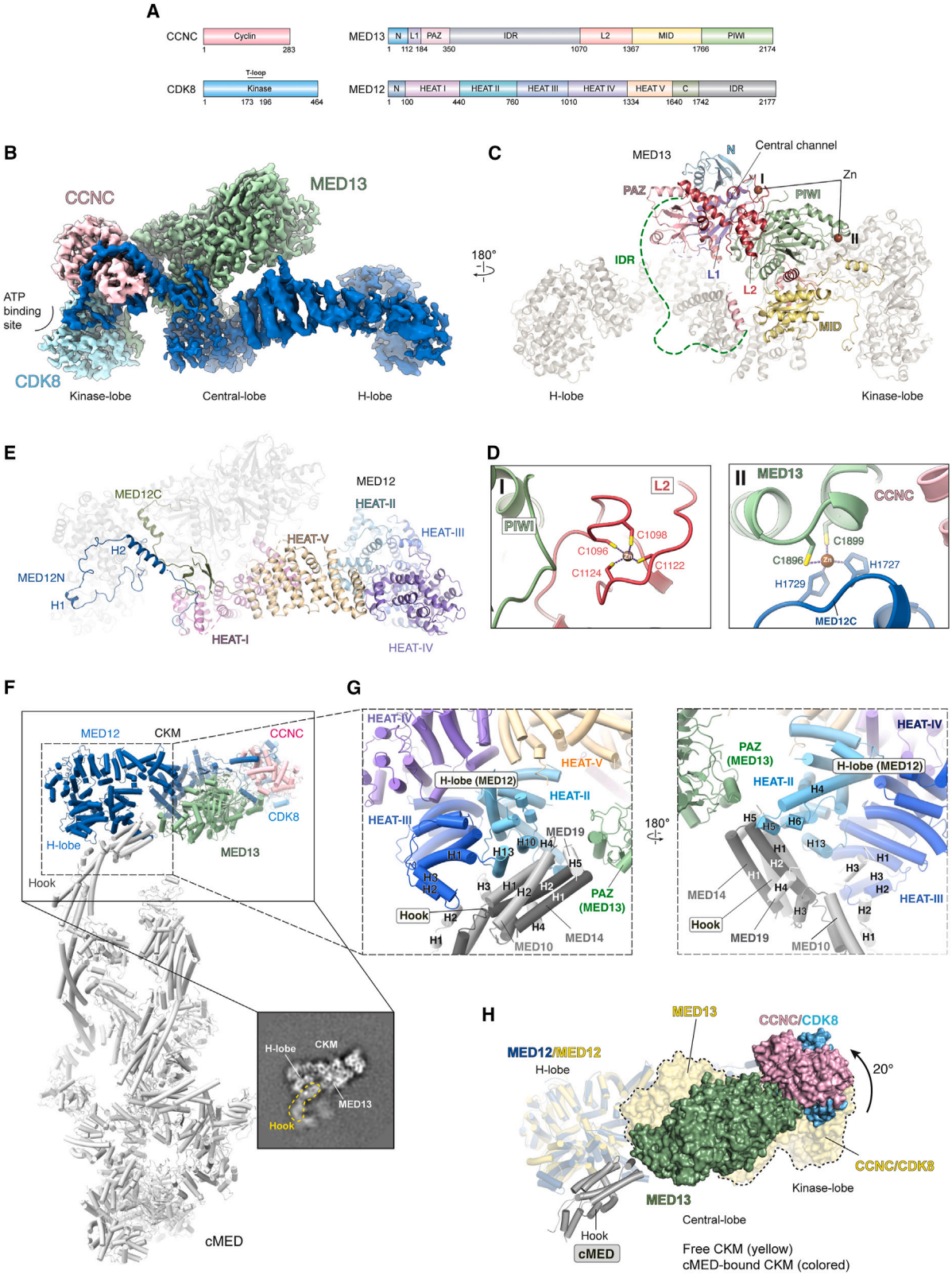

(legend on next page)

Please cite this article in press as: Chao et al., Structural basis of the human transcriptional Mediator regulated by its dissociable kinase module, Molecular Cell (2024), https://doi.org/10.1016/j.molcel.2024.09.001

RESULTS

Structure determination of the complete human Mediator and its dissociable CKM

We purified endogenous Mediator from 293-F cells expressing FLAG-tagged CDK8 through FLAG immunoprecipitation (IP) and glycerol gradient centrifugation (Figures 1B, S1A, and S1B). The purified complex exhibited kinase activity and contained the complete ensemble of Mediator subunits, with the exception of MED26 and CDK19 (Figures S1C and S1D; Data S1). The purified Mediator complex was concentrated to ~1 mg/mL and subjected to structure determination by single-particle cryo-EM (Figure S1E; Table S1).

Two-dimensional (2D) class averages, wherein the cMED portion is aligned, showed CKM binding to the hook of cMED, with a blurred appearance indicating slight CKM mobility (Figure S1F). To investigate the orientation(s) of CKM bound to cMED, we utilized iterative stable alignment and classification (ISAC)[33,34] to generate stable 2D class averages. The resulting averages revealed that CKM adopts a specific orientation when bound to cMED, roughly perpendicular to the long axis of cMED, with no parallel orientations observed (Figures S1G and S1H). Following 2D and three-dimensional (3D) classification, ~105,000 imaged Mediator particles were subjected to 3D reconstruction and refinement, resulting in an ~4.8-Å-density map, whereas the CKM map was blurred out due to its mobility (Figures S2A and S2B). 3D classification produced an overall density map of the Mediator complex at an average resolution of 7.2 Å, clearly showing that the CKM bound to the cMED hook (Figure S2C). Next, 3D maps reconstructed by deep reconstructing generative networks (cryoDRGN)[35] confirmed that the CKM adopts the same approximate perpendicular orientation when bound to cMED, despite positional variability arising from limited mobility of the cMED hook (Figures S3A and S3B). To improve resolution, we divided the Mediator complex into two parts, CKM with the hook (CKM-Hook) and cMED without the hook (cMED-HookΔ), for separate processing. Further focused classification and refinement improved resolution and map quality for cMED-HookΔ (4.7 Å) and CKM-Hook (6.7 Å) (Figures S2D and S2E). Both individually refined maps were then combined into a composite map (Figure 1C).

To better resolve the human CKM structure, particularly due to its limited resolution in cMED-CKM, we used an insect baculovirus expression system to co-express and purify recombinant CKM subunits (Figures S1I and S1J).[18] Purified, enzymatically active CKM was then concentrated and subjected to single-particle cryo-EM (Figures S1C, S1K, and S1N; Table S1). In brief, ~107,000 particle images were obtained using 2D and 3D classifications, followed by particle polishing and 3D refinement, resulting in an overall 3.8-Å cryo-EM map in which the H-lobe showed poor density due to its mobility (Figures S2H and S2I). To improve map quality, the H-lobe and other regions were further classified and refined to 6.5 and 3.6 Å resolutions, respectively (Figures S2J and S2K). An atomic CKM model was built into the cryo-EM density maps using the crystal structure of human CDK8/CCNC[36] and AlphaFold models of MED12 and MED13 as templates[37] (Figure S3D). The atomic model of the complete Mediator complex was built based on global- and focused-refined maps, with the structures of human cMED and CKM as templates (Figures 1D, S3E, and S3F; Table S1).

Architecture of the complete human Mediator

The structure of the Mediator complex reveals a modular architecture, with approximate dimensions of ~460 Å × 210 Å × 160 Å, which contains all Mediator subunits (excluding MED26 and paralogs of CDK8, MED12, and MED13). The complex consists of a large cMED containing head, middle, and tail modules, and an elongated CKM, consisting of kinase-, central-, and H-lobes, at the top (Figure 1D; Video S1). The hook of cMED is bound by the CKM with an orientation that is roughly perpendicular to the middle module (Figures 1D and S1H). The central- and H-lobes of the CKM form direct contacts with the cMED hook, whereas the kinase-lobe at the opposite end of the CKM is positioned distally and away from the cMED, without interacting with other modules. Although the main body of the human CKM primarily utilizes its H-lobe to contact the cMED hook domain, its orientation relative to cMED nonetheless seems to be quite stable, exhibiting only limited mobility, likely due to flexibility in the hook domain (Figures S3A and S3B).

Architecture of human CKM

The human CKM shares the same subunit organization present in its yeast counterpart and has an elongated architecture measuring 210 Å × 50 Å × 85 Å (Figures 2A–2C; Video S2). The kinase-lobe with an ATP-binding site facing outward is mainly comprised of CDK8, CCNC, parts of MED13, and the N terminus of MED12. The central-lobe includes MED13 Ago domains and partial MED12, whereas the H-lobe, formed solely by MED12, consists of tightly packed α helices and exhibits limited conformational variability. MED13 possesses an Ago-like structure with four globular domains (N, PAZ, MID, and PIWI) and two linker regions (L1 and L2) that together form two lobes surrounding a central channel (Figure 2C). Notably, MED13 harbors a large and unique insertion between its

Figure 2. Structure of the human CKM and its interaction with the cMED hook

(A) Domain diagram of CKM subunits.

(B) Composite cryo-EM map of human CKM. The resolutions of the kinase-, central-, and H-lobes are 3.8, 3.6, and 6.5 Å, respectively.

(C) Structure of MED13 (colored) within the CKM. The missing MED13 IDR (residues 350–1,069) is indicated by a dashed line. Other CKM subunits are colored in gray.

(D) Two zinc-binding sites (I and II). Left, Zn^{2+} ion coordinated in MED13. Right, Zn^{2+} ion coordinated between MED13 and MED12.

(E) Structure of MED12 (colored).

(F) CKM bound to the cMED hook. Bottom right: 2D average of CKM bound to hook.

(G) cMED hook-CKM interface.

(H) Conformational changes in the kinase- and central-lobes upon cMED binding. cMED-bound and -free CKM structures were superimposed by aligning their H-lobes.

Please cite this article in press as: Chao et al., Structural basis of the human transcriptional Mediator regulated by its dissociable kinase module, Molecular Cell (2024), https://doi.org/10.1016/j.molcel.2024.09.001

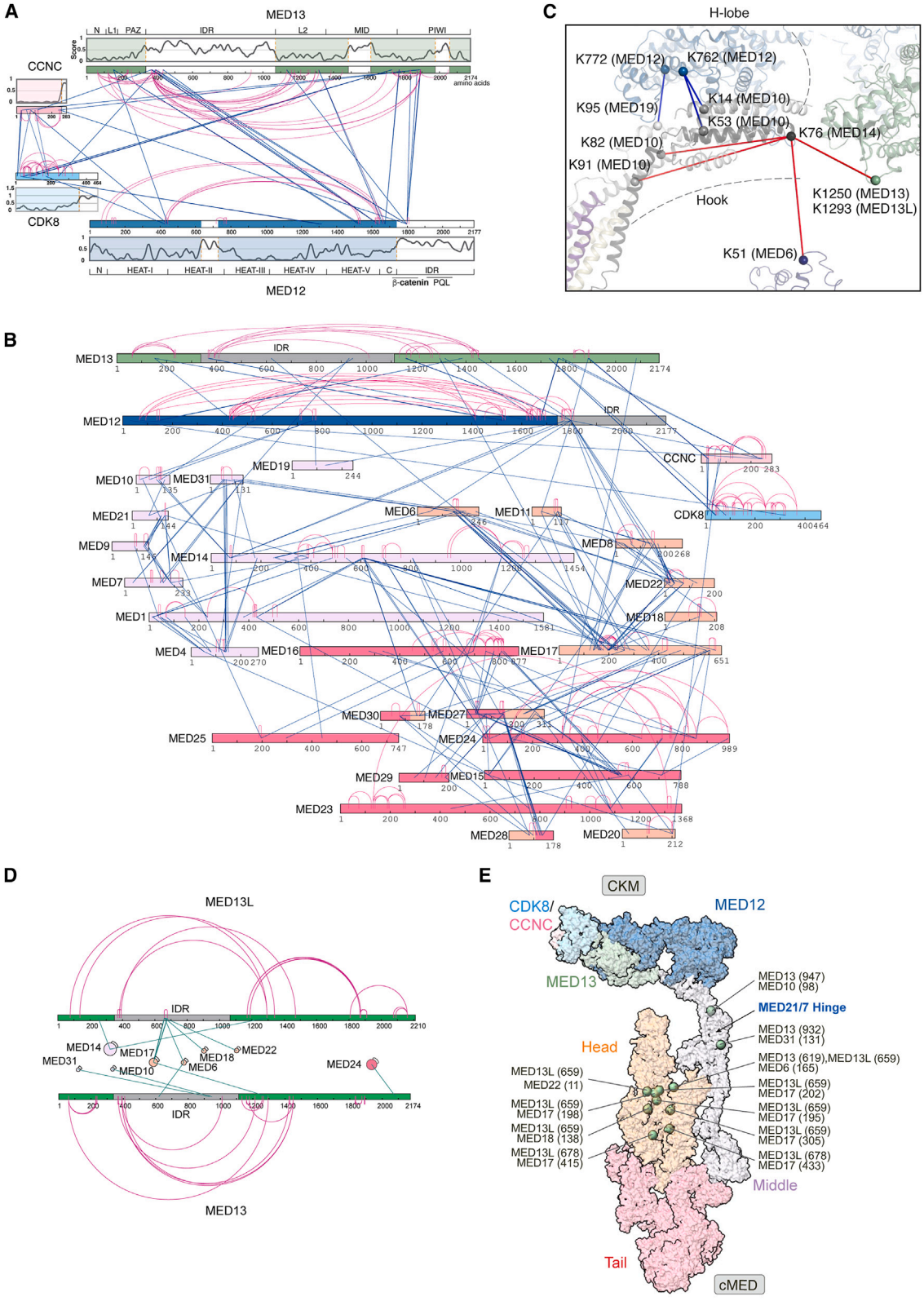

(legend on next page)

Please cite this article in press as: Chao et al., Structural basis of the human transcriptional Mediator regulated by its dissociable kinase module, Molecular Cell (2024), https://doi.org/10.1016/j.molcel.2024.09.001

PAZ and L2 domains, corresponding to its large IDR (residues 350–1,069) (Figures 2A and 2C). Unlike classical Ago proteins in which DNA or RNA is bound in its PAZ and MID domains or central channels,[38,39] no nucleic acid density was observed in MED13. Interestingly, the L2 domain forms a well-organized structure containing several α helices that block the nucleic-acid-binding sites in the PAZ domain and central channel (Figure S4A). Additionally, we identified two zinc-binding sites (I and II), but these were absent in yeast Med13 (Figure 2C). Site I is located on the surface between the L2 and PIWI domains, coordinated by four Cys residues (Figure 2D left). Site II involves two His residues from MED12 and two Cys residues from the MED13 PIWI domain (Figure 2D right). These two zinc-binding sites may contribute to complex stability or protein-protein interactions, and the site II mutation H1729N in MED12 is notably linked to Ohdo syndrome, a rare intellectual disability disorder.[40]

Both the N- and C-terminal portions of MED12 (residues 1–97 and 1,640–1,742, hereafter MED12N and MED12C, respectively) adopt extended conformations connected by five HEAT-repeat domains (HEAT-I to V) (Figure 2E). MED12N contains two α helices that make extensive interactions with CDK8/CCNC. The HEAT-I domain of MED12 lies within the central-lobe and contacts MED13, whereas the remaining four HEAT domains are tightly packed to form the H-lobe. MED12C forms an α helix between the kinase- and central-lobes (Figure 2E). Following MED12C, the proline-, glutamine-, and leucine-rich (PQL) domain (residues 1,763–2,051), known to interact with various transcription factors, including β-catenin, SOX9, and REST, is missing in our density maps.[41,42] In summary, the MED12 N terminus interacts functionally with CDK8/CCNC, whereas the majority of MED12 serves as a structural scaffold, with HEAT domains and unstructured regions providing a large surface area for protein-protein interactions.

Structural analysis of the cMED-CKM interface

The map density at the cMED-CKM interface was initially poor due to flexibility of the cMED hook. Focused image analysis improved map quality, revealing that the interactions are confined to a small region where the hook is primarily bound by the CKM H-lobe, with minor involvement from MED13 (Figures 2F and S3G). The total interaction area is ~680 Å^2. At the top of the hook, H10 and H13 within HEAT-II of the H-lobe contact H1 and H2 of MED10, while H2 of H-lobe HEAT-III interacts with H2 of MED19 (Figure 2G). Near the tip of the hook, MED14 H2 is bound by H5 of H-lobe HEAT-II, while MED19 H5 is slightly contacted by the MED13 PAZ domain (Figure 2G). In this binding mode, CDK8/CCNC is positioned ~120 Å from the hook without contacting cMED (Figure 2F). Together, our structure not only explains early biochemical observations that MED12 and MED13 can associate with MED14 and MED19,[15] respectively, but also uncovers an additional role for the cMED hook in CKM binding. It also shows that the CKM main body predominantly binds to the cMED hook through its MED12 H-lobe. This corrects prior lower-resolution EM studies that incorrectly positioned MED13 as the primary contact subunit with the hook.[9,15] The subunit organization redefined in our recent yeast CKM study[32] aligns with our human CKM structure.

To determine whether cMED or the CKM undergoes structural rearrangements upon their mutual binding, we compared their unbound and bound structures. For the CKM, we found that the kinase- and central-lobes undergo an ~20° rotation relative to the H-lobe upon cMED binding, allowing the hook to engage between the H-lobe and MED13 (Figure 2H). No significant structural rearrangements were observed within cMED, with only subtle conformational changes noted in the tail and middle modules (data not shown).

XL-MS confirms the cMED-CKM-binding mode and reveals a functional role for the MED13 IDR

To support our structural observations, we performed XL-MS analysis on purified free CKM and cMED-CKM (Data S2 and S3). For the CKM, 130 unique residue pairs (URPs) were identified, 69 of which were mapped onto its structure (Figures 3A, S5A, and S5C). These mapped URPs agreed well with the overall architecture and subunit organization of the CKM. Consistent with the CKM structure, the IDRs of MED12 and MED13, which were missing in the density maps, were largely devoid of intersubunit or intrasubunit crosslinks, except for their N-terminal regions (Figure 3A). These findings suggest that, in the absence of cMED, both IDRs adopt flexible, solvent-exposed conformations without stable interactions with the CKM main body.

Regarding the cMED-CKM (i.e., Mediator) complex, we identified 557 URPs, 86 of which were linked to MED12L or MED13L (Figures 3B and S5E). Of the remaining 471 URPs, 277 were mapped onto the cMED-CKM structure (Figures S5B and S5D). The remaining 194 unmapped URPs were found in either unstructured loops or large IDRs. Of the mapped 277 URPs, 214 and 56 occurred within cMED and CKM, respectively. Only 7 URPs were mapped onto the Mediator structure between cMED and the CKM, four of which congregated between the cMED hook and CKM H-lobe or MED13 (Figure 3C). These results support our structural model for human Mediator, wherein the main body of the CKM interacts with the cMED hook through a limited contact area (Figure 1D).

Consistent with localization of the H-lobe next to the cMED hook, specific crosslinks were found between MED12 and MED10/MED19, as well as between MED12L and MED10 (Figures 3C and S5E). Additionally, MED13L was crosslinked to K76 of MED14, which agrees with the localization of MED13

Figure 3. XL-MS analyses of Mediator and its CKM

(A) Crosslinking map and predicted IDRs within the human CKM. Intrasubunit and intersubunit URPs are shown by purple and blue lines, respectively. IDRs identified using IUPred3[43] are based on propensity scores, with residues above 0.5 considered disordered. Regions missing in density maps are colored white.

(B) Crosslinking map of the cMED-CKM.

(C) Crosslinks between MED12 H-lobe/MED13 and cMED hook, with Cα-atoms shown as spheres.

(D) Intrasubunit (purple) crosslinks within MED13/13L and their intersubunit crosslinks (green) with cMED subunits.

(E) Crosslinks between cMED and MED13/13L-IDR are mapped onto the cMED-CKM structure.

next to the hook tip (Figure 3C). Significantly, both CDK8 and CCNC were extensively crosslinked to MED12 and MED13, but not to cMED subunits (Figure 3B), supporting our structural observation that the CKM-cMED hook interaction displaces the kinase-lobe from the main body of cMED (Figure 1D). Nevertheless, we cannot exclude the possibility that a small pool of the CKM may bind to cMED in a distinct manner, based on some of the other identified crosslinks (Figure S5B).

Interestingly, in the presence of cMED, the IDRs of MED13/13L extensively crosslinked with head and middle module subunits of cMED (Figure 3D). In contrast, the MED12 IDR, except for its two N-terminal lysine residues (K1771 and K1798), did not show any crosslinks to cMED, indicating its flexible conformation(s) and lack of stable interactions with cMED. Mapping the URPs of MED13/13L IDRs onto the cMED structure revealed that nearly all of these URPs are clustered at the central region of the head module, with two near the MED21/7 hinge of the middle module (Figure 3E). This suggests that the CKM allocates MED13/13L IDRs to interact with cMED at both its head and middle modules.

The MED13 IDR binds stably to RNA-Pol-II-/MED26-free cMED

MED13 was previously reported to interact with cMED.[9,44] Consistent with this, recombinant full-length MED13 captured cMED proteins present in 293-F cell nuclear extract (Figure 4A). To identify the cMED-binding region (MBR) on MED13, we initially expressed in and purified from insect cells the N-terminal (MED13-N; residues 1–1,320) and C-terminal (MED13-C; residues 1,070–2,174) portions of MED13 (Figure 4B). Pull-down experiments using these two MED13 fragments and 293-F cell nuclear extract revealed that MED13-N, but not MED13-C, bound cMED, thereby delimiting the MBR on MED13 to residues 1–1,069 (Figure 4C left). We then performed glutathione S-transferase (GST) pull-down experiments using smaller MED13 fragments. This analysis revealed that MED13 residues 500–1,069, corresponding to the C-terminal portion of its IDR (hereafter called IDRc), and two derivative fragments therein, residues 500–750 and 840–1,069 (referred as MBR1 and MBR2, respectively), possess cMED-binding capability (Figure 4C right). FLAG-tagged IDRc, ectopically expressed in 293-F cells, was able to co-immunoprecipitate endogenous cMED, forming a stable complex that could be further purified through glycerol gradient centrifugation (Figure 4D). Additionally, the MED13L IDRc (residues 511–1,107) also exhibited cMED interaction ability (Figure 4E). Collectively, these results show that the MED13 IDRc binds directly and stably to cMED.

To characterize proteins associated with the MED13 IDRc, the cMED-containing fractions following glycerol gradient centrifugation were analyzed by mass spectrometric analysis (Data S1). Intriguingly, IDRc-associated proteins included nearly all cMED subunits but neither MED26 nor RNA Pol II, similar to results with FLAG-tagged CDK8 (Figure 4F left and middle). As expected, we observed no other CKM subunits associated with the MED13 IDRc because it possesses no CKM interaction sites. Notably, a FLAG-tagged MED13 derivative lacking the IDRc captured CKM subunits, as expected, but was devoid of cMED (Figure 4G). In contrast, FLAG-tagged MED26-purified proteins contained cMED subunits and RNA Pol II, but not CKM (Figure 4F right). These findings indicate that the IDRc, like the complete CKM, binds cMED in a mutually exclusive manner with RNA Pol II/MED26. To test this, we conducted a pull-down assay using GST-IDRc and 293 cell-derived FLAG-immunoprecipitates, which were obtained through FLAG-tagged MED7, including a mixture of RNA-Pol-II-/MED26-bound and -free cMED complexes. Indeed, we observed that the MED13 IDRc binds only to RNA-Pol-II-/MED26-free cMED (Figure 4H). Altogether, these results reveal an important role for the MED13 IDRc, as well as its mutual exclusivity with RNA Pol II/MED26, in cMED binding.

The CKM main body does not occupy RNA-Pol-II-/MED26-binding sites on cMED

To understand how human CKM inhibits RNA Pol II and MED26 binding to cMED, we docked the CKM structure onto that of the human cMED-PIC (Figure 5A). Intriguingly, the main body of the CKM, when bound to the cMED hook, is located >40Å away from RNA Pol II and MED26 with no overlap. This contradicts a prior model based on yeast studies suggesting that steric hindrance by the CKM main body inhibits RNA Pol II binding, although the exact mechanism remains unclear.[15,32] It is plausible in humans that the CKM precludes RNA Pol II and MED26 association with cMED, not through its main body but rather through the MED13 IDRc, as revealed by our protein-binding analyses (Figure 4). This possibility is further supported by our XL-MS analysis of the cMED-CKM complex that revealed several URPs between the IDRc of MED13/13L and the RNA-Pol-II-/MED26-binding regions on cMED (Figure 5B). For example, within MBR1, K619 of MED13 and K659 and K678 of MED13L were crosslinked to cMED subunits around the neck of the head module, where RNA Pol II binds in the cMED-PIC structure (Figure 5B). Within MBR2, K932 and K947 of MED13 were crosslinked to MED31 and MED10 near the cMED MED21/7 hinge domain, where MED26 binds (Figure 5B). These results suggest that MBR1 and MBR2 of the MED13 IDRc are positioned around the head and middle modules, respectively, to occlude RNA Pol II and MED26 binding.

The CKM dispatches its MED13 IDRc to occupy RNA-Pol-II-CTD- and MED26-binding sites on cMED

To locate potential MED13 IDRc densities within the cMED-CKM structure, we initially used focused 3D classification, refinement, and fitting of the cMED structure into individually refined head, middle, and tail maps (Figures S2F and S2G). Three potential MED13 IDRc densities were observed in the MED21/7 hinge of the middle module, the neck domain of the head module, and the interface between MED6 C-terminal helix (H6) and MED14 (Figures S7A and S7B). To eliminate the possibility that these densities originated from CDK8, CCNC, or MED12, we collected cryo-EM data of MED13 IDRc-bound cMED and determined their structure at an average resolution of 3.7 Å (Figure S6; Table S1). This specimen was confirmed to be completely free of other CKM subunits (Figure 4F left; Data S1).

Within the MED13 IDRc-bound cMED, we observed three IDRc densities: one bound to the middle module, another at the head module, and the third in a region between MED6 C

Please cite this article in press as: Chao et al., Structural basis of the human transcriptional Mediator regulated by its dissociable kinase module, Molecular Cell (2024), https://doi.org/10.1016/j.molcel.2024.09.001

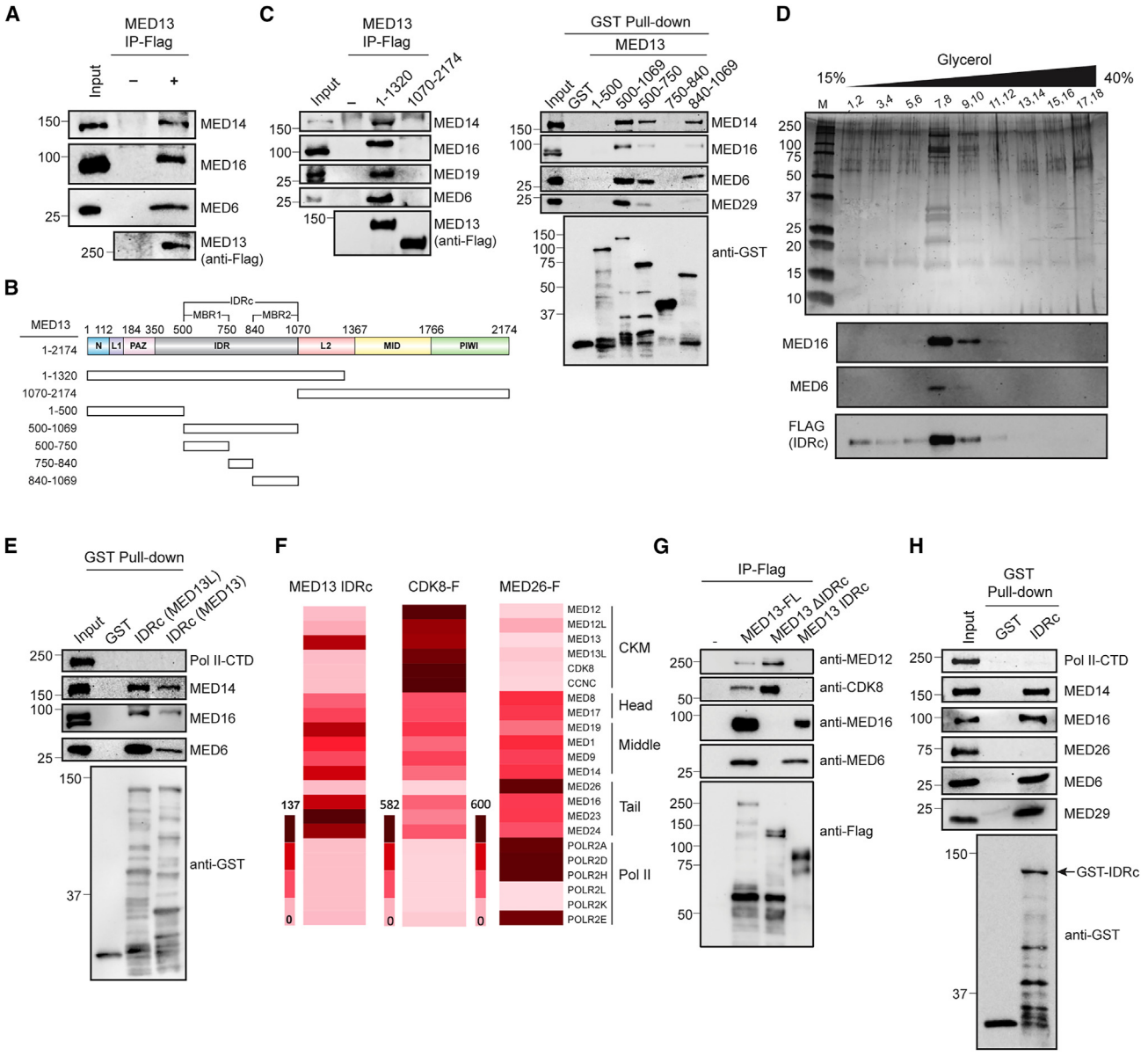

Figure 4. MED13 uses its IDRc to interact with cMED

(A, C, E, G, and H) Pull-down analyses.

(A) FLAG-tagged MED13 immobilized on anti-FLAG beads was used to pull down cMED proteins from 293-F cell nuclear extract (NE).

(B) MED13 fragments used for cMED interaction analysis.

(C) Left, the N-terminal portion (residues 1–1,320) of MED13 associates with cMED. Right, the IDRc, MBR1, and MBR2 of MED13 interact with cMED.

(D) Glycerol gradient centrifugation analysis of purified MED13-IDRc-bound cMED. Gradient fractions were analyzed by SDS-PAGE, with silver staining (top) and immunoblotting using indicated antibodies (bottom).

(E) MED13/13L IDRc associate with cMED proteins from 293-F NE.

(F) Mass spectrometric analysis. Heatmap showing scaled abundance of cMED, CKM, and RNA Pol II proteins purified via FLAG-tagged MED13 IDRc, CDK8, or MED26.

(G) MED13 IDRc interacts with cMED, but not CKM, subunits. MED13 with IDRc truncation cannot interact with cMED.

(H) MED13 IDRc-bound cMED does not contain RNA Pol II/MED26. GST-MED13 IDRc was used to capture cMED proteins isolated from HEK293 NE.

terminus and the knob domain (Figure 5C). Notably, these positions are consistent with those observed in the cMED-CKM density map (Figures S7B and S7C). In the middle module, the IDRc density starts below the knob next to MED7 by forming a small helix bound to the MED7/21 hinge and then runs as a coil toward the base of the hook region through multiple contacts with MED21 (Figure 5D). The IDRc density at this position agrees with two URPs: K932 and K947 of MED13, crosslinked to K131

Please cite this article in press as: Chao et al., Structural basis of the human transcriptional Mediator regulated by its dissociable kinase module, Molecular Cell (2024), https://doi.org/10.1016/j.molcel.2024.09.001

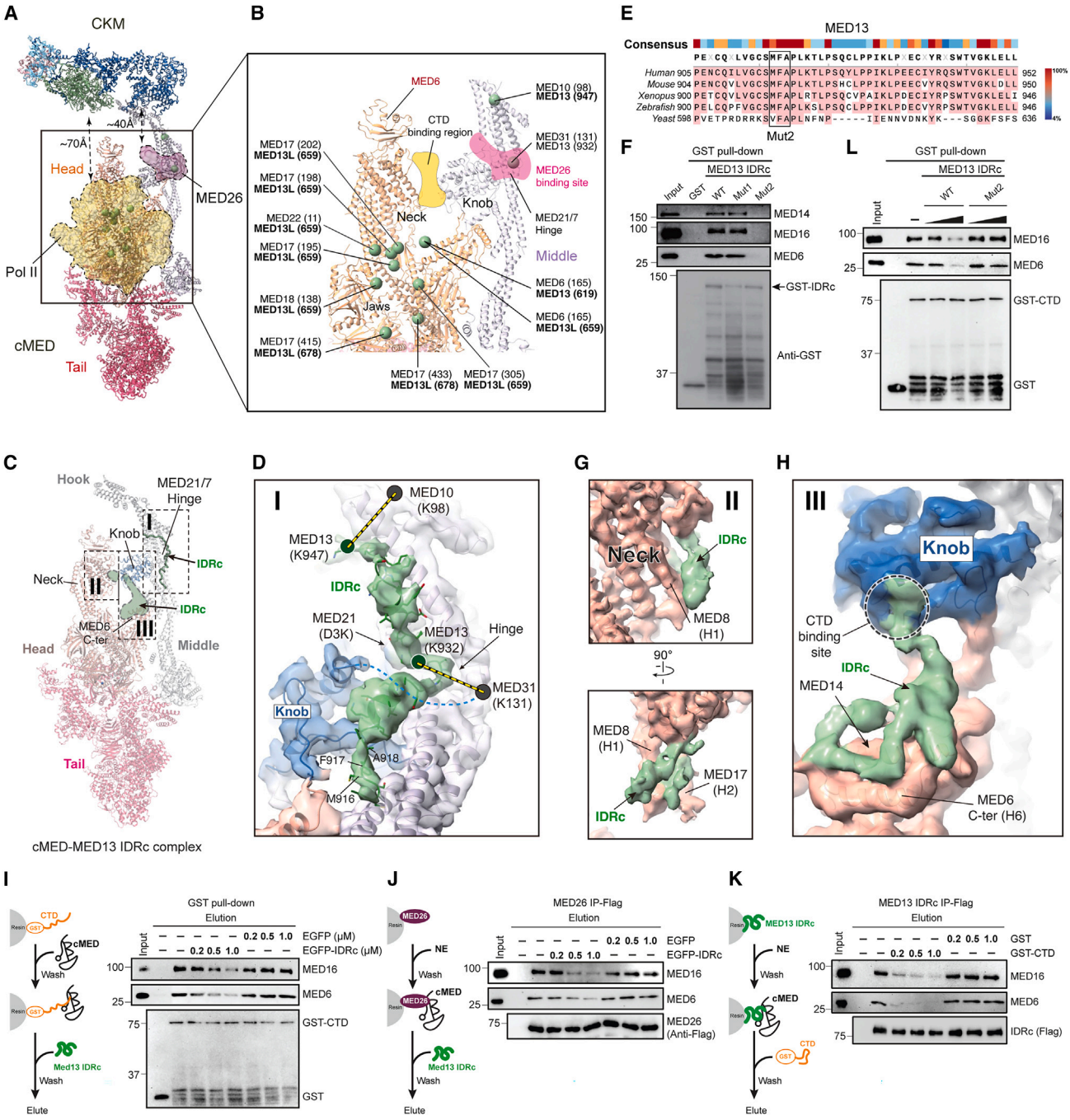

Figure 5. MED13 IDRc excludes RNA Pol II/MED26 interactions with cMED by occupying their binding sites

(A) The CKM main body does not overlap with RNA-Pol-II-/MED26-binding sites on cMED, but URPs (green) with MED13/13L IDRc do.

(B) Crosslinks between cMED and MED13/13L IDRc are mapped onto the cMED-CKM structure.

(C) Structure of the MED13 IDRc-bound cMED complex. Three IDRc-binding sites (I–III) on cMED are indicated.

(D) MED13 IDRc (green density) bound to the MED21/7 hinge (I) of cMED.

(E) Sequence alignment of a conserved region within the MBR2 of MED13 IDRc.

(F) Pull-down experiment showing that GST-IDRc WT and Mut1, but not Mut2, interact with cMED proteins from 293-F NE. Mut1: F847D/S848Y/P849D. Mut2: M916D/F917D/A918Y.

(G) MED13 IDRc bound to the neck of head module (II).

(H) MED13 IDRc bridges the MED6 C terminus and the knob domain (III).

(legend continued on next page)

Please cite this article in press as: Chao et al., Structural basis of the human transcriptional Mediator regulated by its dissociable kinase module, Molecular Cell (2024), https://doi.org/10.1016/j.molcel.2024.09.001

of MED31 and K98 of MED10, respectively (Figure 5D). We were able to assign amino acids (residues 915–949) of MED13 into this density (Figure 5D). Interestingly, this modeled segment, containing two motifs, SMFAPL and GKL, exhibits a high degree of sequence conservation among species, especially in vertebrates, suggesting a conserved functional role in cMED binding (Figure 5E). To test this, we introduced a triple mutation (M916D/F917D/A918Y; Mut2) within the SMFAPL motif of IDRc, significantly altering the amino acid charges or characteristics, and examined its impact on cMED binding using a pull-down experiment. Our results showed that IDRc Mut2 was significantly impaired for its interaction with cMED (Figure 5F). By contrast, an unrelated triple mutation (F847D/S848Y/P849D; Mut1) located between MBR1 and MBR2 had no impact on the IDRc-cMED interaction (Figure 5F). These results support our structural and XL-MS findings that the conserved region (residues 915–949) within the IDRc is crucial for MED21/7 hinge binding.

For the other two IDRc densities, residues were not assigned due to conformational heterogeneity. One is positioned next to the H1 of MED8 and H2 of MED17 in the neck of the head module (Figure 5G), while the other forms a continuous density, extending from the interface between the H6 of MED6 and MED14 toward the knob domain of the middle module (Figure 5H). Because the RNA Pol II CTD is bound between the head and middle modules[25,27,29,31,45,46] (Figure S7D), we investigated the possibility that the IDRc overlaps with the CTD by aligning structures of the human and yeast cMED-PIC with our model. Strikingly, we found that IDRc densities in the neck of the head module clash with the N-terminal regions of the CTD in both human and yeast structures of cMED-PIC (Figures S7E and S7F). Furthermore, the IDRc density next to MED6C H6 extends toward to the knob domain, where it coincides with the N terminus of the observed CTD within human cMED-PIC (Figure S7G). Because the cMED-RNA Pol II interaction is mediated by the CTD engaged between the neck and knob domains following cMED structural rearrangements,[25,27,29] the IDRc bound to the neck and knob regions could preclude both CTD binding as well as CTD-induced cMED conformational changes. On the other hand, the MED13 IDRc bound at the MED21/7 hinge also significantly coincides with the CTD of MED26 (Figure S7H). All of these structural observations suggest that the MED13 IDRc can compete with the RNA Pol II CTD and MED26 for binding to cMED by inducing steric hindrance.

The MED13 IDRc competes with RNA Pol II CTD and MED26 for cMED binding

To further investigate the influence of the MED13 IDRc on interactions between RNA Pol II CTD, MED26, and cMED, we conducted competitive binding assays. We added increasing amounts of purified EGFP-tagged IDRc to either CTD- or MED26-bound cMED and monitored remaining cMED levels after washing (Figures 5I and 5J). Results showed that cMED bound to beads through CTD or MED26 was competed off by EGFP-tagged MED13 IDRc, but not by EGFP alone, in a concentration-dependent manner. Reciprocally, cMED bound to beads through MED13 IDRc was competed off by excess GST-CTD, but not GST alone (Figure 5K). Additionally, a cMED-binding-defective IDRc mutant derivative (M916D/F917D/A918Y; Mut2) failed to compete with RNA Pol II CTD for cMED binding (Figure 5L). Altogether, these results support our structural observations, demonstrating that the MED13 IDRc occludes RNA Pol II CTD and MED26 binding to cMED. This explains why Mediator proteins purified through the MED13 IDRc contain neither MED26 nor RNA Pol II (Figure 4F left) and, further, why a MED21 D3K mutation (Asp3 to Lys in MED21) within the cMED hinge was previously reported to disrupt both MED26 and MED13 binding[47] (Figure 5D). In summary, our results reveal the MED13 IDRc to be a key determinant of the mutual exclusivity between CKM and RNA Pol II/MED26 in cMED binding.

MED13 IDRc represses cMED-dependent transcription

To assess the impact of MED13 IDRc on cMED-dependent transcription, we examined how IDRc expression affects transcription driven by the VP16 activation domain, which recruits cMED through its MED25 subunit.[48,49] As expected, Gal4-VP16 conferred high-level expression of a luciferase reporter gene controlled by Gal4 responsive elements in human HEK293 cells (Figure 6A). Notably, ectopic expression of MED13 IDRc repressed Gal4-VP16-driven luciferase activity in a dose-dependent manner, similar to full-length MED13, a known repressor of activator-dependent transcription in mammalian cells[50] (Figure 6A). We also examined the impact of the IDRc on RNA Pol II transcription using an "artificial recruitment" assay based on the ability of promoter-bound Gal4-MED26 to conscript cMED.[14] Notably, Gal4-MED26-driven reporter gene activation was inhibited in a dose-dependent manner by ectopic expression of both full-length wild-type (WT) MED13 and its IDRc (Figure 6B), but not by IDRc derivatives carrying structurally guided mutations at residues within its overlapping MED26-binding site (Figure 6C). Similarly, full-length MED13 Mut2 (M916D/F917D/A918Y), a cMED-binding-defective derivative, did not significantly inhibit Gal4-MED26-driven luciferase expression compared with WT MED13 (Figure 6D). These results suggest that MED13 IDRc competitively inhibits cMED recruitment by Gal4-MED26, leading to dose-dependent transcriptional repression. Notably, the MED13 and MED13L IDRs share moderate sequence identity of approximately 41%. We found that the MED13L IDRc (residues 511–1,107) is similarly proficient in repressing activator-driven reporter gene activation (Figures 6E and 6F). Altogether, these functional studies confirm our structural and biochemical findings that the MED13/13L IDRc competes with RNA Pol II/MED26 for cMED and plays a role in repressing cMED-dependent transcription.

(I–L) Competitive binding assays. Protein concentrations (μM) used in competition are indicated. Eluted proteins were detected by western blotting using specified antibodies.
(I and J) MED13 IDRc competes with RNA Pol II CTD or MED26 for cMED binding.
(K) GST-CTD competes with MED13 IDRc for cMED binding.
(L) WT MED13 IDRc, but not Mut2, competes with GST-CTD for cMED binding.

Please cite this article in press as: Chao et al., Structural basis of the human transcriptional Mediator regulated by its dissociable kinase module, Molecular Cell (2024), https://doi.org/10.1016/j.molcel.2024.09.001

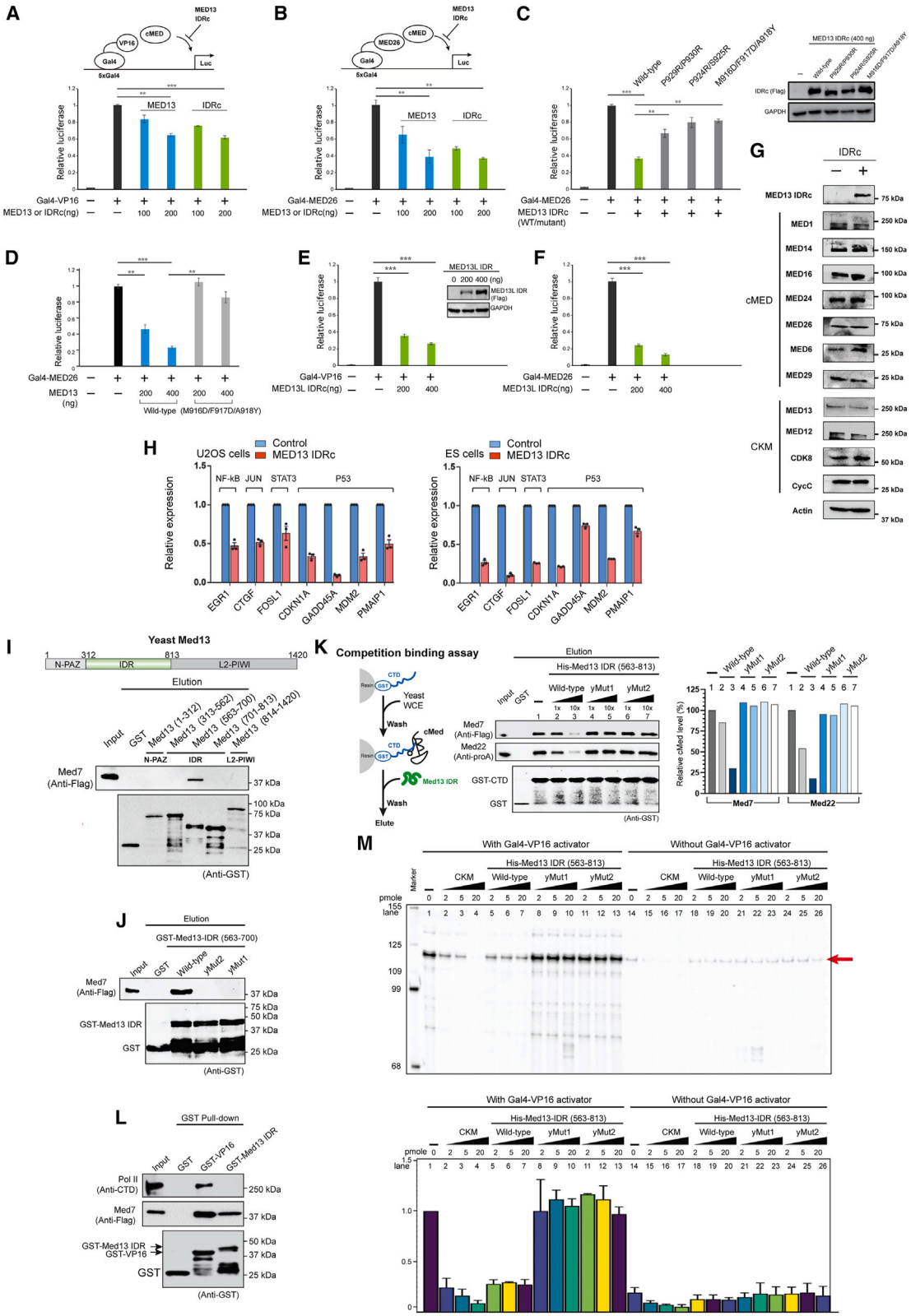

(legend on next page)

Please cite this article in press as: Chao et al., Structural basis of the human transcriptional Mediator regulated by its dissociable kinase module, Molecular Cell (2024), https://doi.org/10.1016/j.molcel.2024.09.001

To investigate whether the MED13 IDRc can influence gene expression in human cells, we conducted quantitative reverse-transcription PCR (RT-qPCR) experiments in human osteosarcoma U2OS and embryonic stem (ES) cell lines following lentiviral-based overexpression of the IDRc. Notably, IDRc expression did not significantly alter endogenous Mediator protein levels (Figure 6G). We examined the homeostatic expression of genes regulated by transcription factors, including nuclear factor κB (NF-κB), JUN, STAT3, and p53, previously reported to involve cMED, for their function (Figure 6H). Compared with a control virus, IDRc expression resulted in the downregulation of multiple target genes, including EGR1, CTGF, FOSL1, GADD45, MDM2, and PMAIP1. These results indicate that MED13 IDRc can repress target gene expression by influencing the interaction of RNA Pol II with cMED, which is recruited by each of their cognate transcription factors.

Yeast Med13 IDR binds cMed, prevents RNA Pol II binding, and inhibits cMed-dependent transcription

To map the MBR on Med13, we assessed the ability of bead-immobilized GST-Med13 fragments spanning its entire length to capture cMed present in yeast whole-cell extract (WCE). Strikingly, we found that GST-Med13 (563–700) was alone responsible for cMed binding (Figure 6I). Notably, this cMED-binding domain within the Med13 IDR harbors a small region (residues 598–636) that aligns well with a cMED-hinge-binding fragment (residues 905–952) within the human MED13 IDRc; this region is highly conserved among vertebrate MED13 proteins and includes two motifs, SMFAPL and GKL, which are also conserved in yeast Med13 (Figure 5E). To test whether these motifs mediate binding of Med13 to cMed, we generated two GST-Med13 (563–700) mutants (V609D/F610D/A611K [yMut2] and G630R/G631R/K632E [yMut1]) and assessed their respective abilities to capture cMed from yeast whole-cell extract. Compared with GST-Med13 (563–700) WT, both mutants were severely compromised for cMed association, establishing these two Med13 IDR conserved motifs as important determinants of cMed binding (Figure 6J).

To assess the impact of yeast Med13 IDR on the interaction between RNA Pol II CTD and cMed, we conducted competitive binding assays. Accordingly, we comparatively assessed the ability of WT Med13 IDR and each of its two cMed-binding-defective mutants, when added at increasing amounts, to block the interaction of cMed with bead-immobilized GST-CTD. This analysis revealed that WT Med13 IDR, like its human counterpart, significantly and in a concentration-dependent manner hindered the binding of cMed to GST-CTD, whereas neither IDR mutant could do so (Figures 6K and S1P). Additionally, we probed for the presence of RNA Pol II and/or cMed among proteins captured from yeast whole-cell extract by GST-VP16 or GST-Med13 IDR. We found that the VP16 activation domain bound cMED in association with RNA Pol II, whereas the Med13 IDR bound only cMed free of RNA Pol II (Figure 6L). Altogether, these results support a model wherein the Med13 IDR blocks the association of RNA Pol II with cMED by direct occlusion of its CTD-binding interface therein.

To investigate the impact of the Med13 IDR on cMed-dependent transcription, we employed *in vitro* transcription in yeast whole-cell extracts using purified Gal4-VP16 activator and a Gal4-SNR20 promoter DNA template, where transcription activation is dependent on the activator protein and Mediator[31] (Figure 6M lanes 14 and 1). Notably, addition of purified yCKM led to a dose-dependent inhibition of cMed-dependent transcription driven by Gal4-VP16 (Figure 6M lanes 2–4). Strikingly, although WT Med13 IDR similarly inhibited Gal4-driven transcription, albeit to a lesser extent than CKM, neither of its two cMED-binding-defective mutants could do so (Figure 6M lanes 5–13), implying that the IDR exerts its inhibitory influence on activator-driven transcription by impeding the interaction between cMed and RNA Pol II. Notably, only 2 pmol (62 nM) of WT Med13 IDRc or CKM was sufficient to completely suppress activator-dependent transcription to the basal level (Figure 6M, lanes 5–7). Remarkably, neither WT nor mutant Med13 IDR derivatives inhibited basal (activator-independent) transcription from the same DNA template (Figure 6M lanes 18–26), supporting the notion that the inhibitory activity of the IDR is exerted through cMed. Altogether, the role of human MED13 IDRc in transcription repression, by impeding the interaction between cMED with RNA Pol II, is likely conserved in yeast.

Figure 6. MED13 IDRc represses cMED-dependent transcription

(A–F) Luciferase reporter assays. Data plots represent relative luciferase activity from the average of triplicate independent transfections (*$p < 0.05$; **$p < 0.01$; ***$p < 0.001$).

(A) Inhibition of Gal4-VP16-driven 5xGal4-TATA-luc (Gal4-Luc) reporter by MED13 and its IDRc.

(B) Inhibition of Gal4-MED26-driven Gal4-Luc reporter by MED13 and its IDRc.

(C) Inhibition of Gal4-MED26-driven Gal4-Luc reporter by WT MED13 IDRc and its mutants.

(D) Inhibition of Gal4-MED26-driven Gal4-Luc reporter by WT MED13 and its (M916D/F917D/A918Y) mutant.

(E and F) Inhibition of Gal4-MED26- or Gal4-VP16-driven Gal4-Luc reporter by MED13L IDRc.

(G) Immunoblot analysis comparing expression levels of cMED and CKM subunits in the absence and presence of overexpressed MED13 IDRc in U2OS cells.

(H) RT-qPCR analysis of genes regulated by the indicated transcription factors in human U2OS or ES cells transduced with control or MED13 IDRc-expressing lentiviruses. Relative expression levels are plotted based on three independent experiments.

(I) Top, domain diagram of yeast Med13. Bottom, GST pull-down analysis using yeast Med13 fragments identifies one region (residues 563–700) within the IDR that binds cMed from whole-cell extract (WCE).

(J) GST pull-down analysis reveals interaction of WT, but not mutant, Med13 IDR with cMed from yeast WCE. yMut1: V609D/F610D/A611K; yMut2: G630R/G631R/K632E.

(K) Competitive binding assay. Yeast WT Med13 IDR, but not its mutants, competes with RNA Pol II CTD for cMed binding. Eluted proteins were detected by immunoblot, quantified, and normalized based on band intensities.

(L) GST-tagged VP16 or Med13 IDR was used to pull down cMed proteins from WCE.

(M) Top, yeast *in vitro* transcription assay showing activator-dependent transcription repressed by CKM and WT Med13 IDR, but not by Med13 IDR mutants. Bottom, specific transcripts (indicated by a red arrow) were quantitated and normalized based on band intensities.

Please cite this article in press as: Chao et al., Structural basis of the human transcriptional Mediator regulated by its dissociable kinase module, Molecular Cell (2024), https://doi.org/10.1016/j.molcel.2024.09.001

CellPress

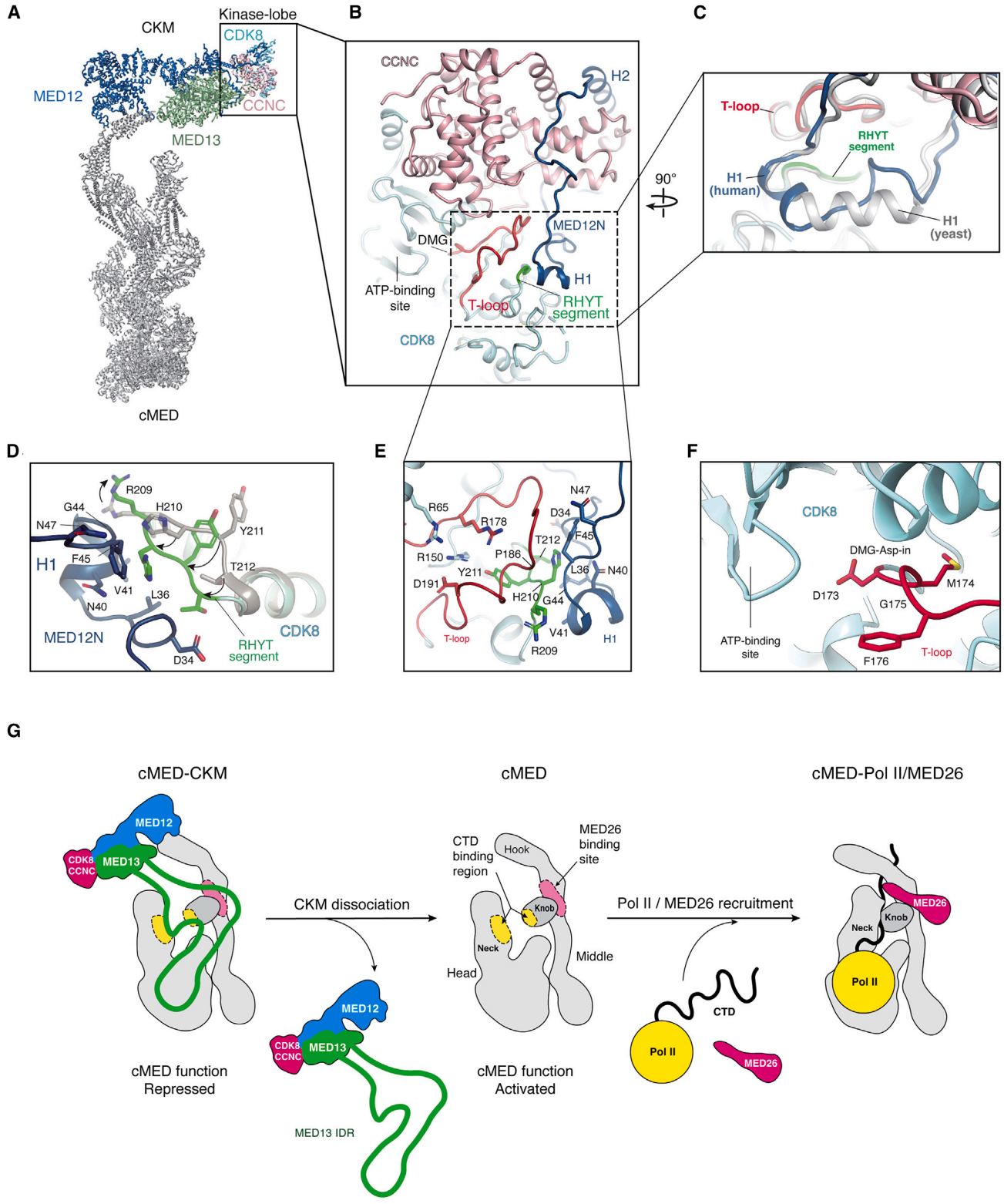

Figure 7. MED12-dependent CDK8 activation mechanism and proposed model for CKM-mediated transcription repression

(A) Position of CDK8/CCNC in the Mediator complex.

(B) CDK8/CCNC bound by MED12N (blue), with the CDK8 T-loop in red and RHYT in green.

(C) Human MED12N adopts a different conformation from yeast (PDB: 7KPX) for CDK8 activation. Human MED12N is blue, yeast is white.

(legend continued on next page)

Please cite this article in press as: Chao et al., Structural basis of the human transcriptional Mediator regulated by its dissociable kinase module, Molecular Cell (2024), https://doi.org/10.1016/j.molcel.2024.09.001

CDK8 activation by MED12

Within the kinase-lobe of human CKM, MED12N adopts an extended conformation, enabling it to contact CDK8 near the T-loop through a short α helix H1 and its flanking regions (Figures 7A and 7B). Unlike the N-terminal region of yeast Med12 that uses a long activation α helix to alter the conformation of the RHYT segment of CDK8,[51] the corresponding region in human MED12 instead adopts a coil structure followed by a short α helix H1 to activate CDK8 (Figures 7C and S4C). To achieve this, the RHYT segment of human CDK8 undergoes a structural rearrangement induced by several contacts with the main chain of N40 and V41 of MED12 H1, as well as adjacent MED12 residues, D34, L36, and G44 (Figures 7D and S4B). These interactions alter the side chain orientation of Y211 in the RHYT segment, enabling a precise network of intramolecular interactions with the CDK8 T-loop (Figure 7E). Thus, the T-loop is well-defined in the density map (Figure S3D) and assumes an activated conformation in which residues 173–175, next to the ATP-binding site, adopt a "DMG-Asp-in" state (Figure 7F). Taken together, the CDK8 activation mechanism remains conserved between yeast and humans, involving stabilization of the T-loop through Y211 in the rearranged RHYT segment.

DISCUSSION

It has been shown that human CKM can repress transcription independently of its CDK8 kinase activity.[9,52] Based on low-resolution structural information from yeast Mediator, steric hindrance involving occlusion of the RNA-Pol-II-binding site on cMed by the CKM main body has been considered a possible mechanism for CKM-mediated transcriptional repression.[15,21] In our human Mediator structure, the main body of the CKM adopts a relatively stable orientation in contrast to yeast CKM and neither overlaps with RNA Pol II/MED26 nor induces apparent cMED structural rearrangements. Strikingly, we find instead that the MED13 IDRc blocks interaction of RNA Pol II CTD and MED26 with cMED by direct occlusion of their corresponding binding sites, revealing a hitherto unknown role for the MED13 IDRc as a modulator of cMED function (Figure 7G). Prior studies have shown that MED26 is implicated in TFIID and/or SEC recruitment[14] and is essential for cMED-dependent transcription *in vitro*.[53] Therefore, by blocking the binding of MED26 to cMED, the MED13 IDRc may, in addition to inhibition of RNA Pol II recruitment, impose an additional layer of regulation upon cMED-dependent gene expression. Accordingly, dissociation of the MED13 IDR from cMED should be a critical regulatory step prior to RNA Pol II binding or cMED-PIC formation in the transcription initiation process (Figure 7G). Post-translational modifications (PTMs), including MED13 ubiquitination and/or phosphorylation as previously reported, represent possible ways to remove the MED13 IDRc from cMED.[54–56]

Within the CKM structure, the ordered regions of MED12 and MED13 exhibit high sequence identity with their paralogs. AlphaFold models of MED12L and MED13L can be well-superimposed onto the cryo-EM structures of MED12 and MED13, respectively, except for the N- and C-terminal regions of MED12/12L and the IDRs of MED13/13L. Accordingly, the overall structures, cMED-binding modes, and CDK8 activation mechanism ascribed to MED12 and MED13 are likely similar to those of their paralogs.

Human CKM has been extensively linked to disease.[57,58] Our human CKM structure not only confirms the importance of the MED12 N terminus in both binding and activation of CDK8 but also provides a structural framework to assess the effects of disease-causing mutations on CKM function (Figure S4D).[57] Uterine fibroid hotspot mutations in MED12[59] are highly clustered within or adjacent to H1 and critically interface with the CDK8 RHYT/T-loop region, providing a structural basis to explain the deleterious impact of these mutations on MED12-dependent CDK8 activation.[18,60,61] In the human CKM structure, MED12 G44 that contacts the RHYT segment is next to the T-loop (Figure 7E). Accordingly, G44 mutations are likely to alter the T-loop and RHYT segment through their side chains, leading to impaired kinase activity, which explains why G44 is the most frequently mutated residue in uterine fibroids (Figure S4E).[18,57]

In summary, the CKM regulates cMED function by suppressing its activity through MED13 IDRc, blocking RNA Pol II CTD/MED26 binding and influencing transcription initiation. We found that the IDRs of both yeast and human MED13 compete with RNA Pol II CTD for cMED binding, leading to a conserved repression mechanism. However, CDK8 within the CKM can also enhance gene transcription, though the underlying mechanisms require further investigation.

Limitations of the study

Due to conformational heterogeneity in the MED13 IDRc, its densities at the neck region of the head and the interface between MED6C and knob were not modeled. Because overexpressed MED13 IDR may compete with endogenous MED13 for cMED binding, functional analyses based on reporter and gene expression assays might not fully reflect direct effects of the IDRc. Considering that the dissociation of MED13 IDRc from cMED likely serves as a crucial regulatory step preceding RNA Pol II binding or cMED-PIC formation during transcription initiation, exploring the mechanisms behind this process holds significant interest.

RESOURCE AVAILABILITY

Lead contact

Further information and requests for reagents should be directed to and will be fulfilled by the lead contact, Kuang-Lei Tsai (Kuang-Lei.Tai@uth.tmc.edu).

(D) The RHYT segment (white) undergoes structural rearrangement (green) upon MED12N binding.
(E) CDK8 T-loop and RHYT segment contacted by MED12N.
(F) T-loop in the "DMG-Asp-in" conformation indicates active CDK8.
(G) Model of CKM-mediated transcription repression. Before transcription initiation, CKM dispatches MED13 IDRc to block RNA-Pol-II-CTD-/MED26-binding sites on cMED, inhibiting cMED-PIC formation and keeping cMED repressed. CKM dissociation permits RNA Pol II/MED26 binding, enabling cMED-PIC formation and transcriptional activation. Tail module omitted for clarity.

Materials availability

Plasmids generated in this study are available upon request from the lead contact with a completed Materials Transfer Agreement.

Data and code availability

- Cryo-EM maps of the human cMED-CKM, CKM-Hook, head-IDR, and middle-IDR were deposited to the EMDataBank, with accession numbers EMDataBank: EMD-41565, EMD-41509, EMD-41511, and EMD-41507, respectively. The cMED-CKM model built based on these maps were deposited to the Protein Data Bank, with an accession number PDB: 8TQW. Cryo-EM maps of the human CKM, kinase-lobe, kinase/central-lobes, and H-lobe were deposited to the EMDataBank, with accession numbers EMDataBank: EMD-41502, EMD-41499, EMD-41500, and EMD-41497, respectively. The CKM model built based on these maps was deposited to the Protein Data Bank, with an accession number PDB: 8TQC. Cryo-EM maps of the human cMED-MED13 IDRc, head-MED13 IDRc, and middle-MED13 IDRc were deposited to the EMDataBank, with accession numbers EMDataBank: EMD-41580, EMD-41512, and EMD-41513, respectively. The cMED-MED13 IDRc model built based on these maps was deposited to the Protein Data Bank, with an accession number PDB: 8TRH. The raw data and analysis results from the XL-MS of human CKM and cMED-CKM have been deposited in ProteomeXchange, with an accession number ProteomeXchange: PXD044328. Original gel and western blot images have been deposited at Mendeley Database and are publicly available as of the publication date, accessible via the DOI provided in the key resources table.
- This paper does not report original code.
- Any additional information required to reanalyze the data reported in this paper is available from the lead contact upon request.

ACKNOWLEDGMENTS

We thank the Structural Biology Imaging Center at UTHealth McGovern Medical School for cryo-EM data collection and the mass spectrometry facilities at the University of Pennsylvania, UTHealth Science Center, and Baylor College of Medicine for XL-MS analysis and protein identification. Gal4-VP16 activator and reporter plasmids were kindly provided by M. Carey (UCLA). This work was supported by the Cancer Prevention Research Institute of Texas, grant number 13127 to CPRIT Scholar in Cancer Research Kuang-Lei Tsai, and grant number RP190602 to CPRIT core facility; the Welch Foundation (AU-2050-20200401); US National Institutes of Health grants R01 GM143587 (K.-L.T.), R01 HD087417 and HD094378 (T.G.B.), R01 GM123233 (K.M.), R01 CA246130 and R01 HL142704 (D.-F.L.), NIH NRSA F31AG069390 (H.J.K.), and NIH F31GM147945 (L.P.); and Biomedical Informatics, Genomics, and Translational Cancer Research Training Program (BIG-TCR) CPRIT RP210045 (S.-F.C.).

AUTHOR CONTRIBUTIONS

S.-F.C., T.-C.C., H.-C.T., and S.K. purified and prepared the human CKM specimen for structural determination. T.-C.C., and H.-C.T. handled the purification and preparation of human cMED-CKM and cMED-MED13 IDRc specimens. S.-F.C., T.-C.C., and K.-L.T. conducted cryo-EM analysis. H.J.K., L.P., and K.M. performed XL-MS and conducted yeast transcription assays. T.-C.C., A.X., M.-F.H., and D.-F.L. carried out RT-qPCR. T.-C.C., S.-F.C., and T.L. performed sequence analyses and structural comparisons. S.-F.C., T.-C.C., and H.-C.T. performed binding assays and kinase activity measurements. K.M., T.G.B., and K.-L.T. supervised the project. Both T.-C.C. and S.-F.C. contributed equally and may list their name foremost on their CV. All authors discussed and interpreted the results. The manuscript was written by T.-C.C., S.-F.C., K.M., T.G.B., and K.-L.T.

DECLARATION OF INTERESTS

The authors declare no competing interests.

STAR★METHODS

Detailed methods are provided in the online version of this paper and include the following:

- KEY RESOURCES TABLE
- EXPERIMENTAL MODEL AND STUDY PARTICIPANT DETAILS
- METHOD DETAILS
  - Cell culture
  - Purification of human cMED-CKM and MED13 IDRc-bound cMED
  - Expression and purification of recombinant human CKM
  - Expression and purification of recombinant human MED13 proteins
  - GST pull-down assay
  - FLAG immunoprecipitation
  - Negative stain EM
  - Cryo-EM specimen preparation, data collection, and image analysis
  - Model building and refinement
  - *In vitro* kinase assay
  - XL-MS analyses of the CKM and cMED-CKM
  - LC-MS-MS analyses of purified Mediator proteins
  - Competitive binding assays
  - Mapping of cMed interaction region on yeast Med13
  - Luciferase reporter assays
  - RT-qPCR
  - Yeast transcription assay
- QUANTIFICATION AND STATISTICAL ANALYSIS

SUPPLEMENTAL INFORMATION

Supplemental information can be found online at https://doi.org/10.1016/j.molcel.2024.09.001.

Received: March 28, 2023
Revised: January 5, 2024
Accepted: September 3, 2024
Published: September 24, 2024

REFERENCES

1. Kornberg, R.D. (2005). Mediator and the mechanism of transcriptional activation. Trends Biochem. Sci. *30*, 235–239. https://doi.org/10.1016/j.tibs.2005.03.011.
2. Malik, S., and Roeder, R.G. (2010). The metazoan Mediator co-activator complex as an integrative hub for transcriptional regulation. Nat. Rev. Genet. *11*, 761–772. https://doi.org/10.1038/nrg2901.
3. Soutourina, J. (2018). Transcription regulation by the Mediator complex. Nat. Rev. Mol. Cell Biol. *19*, 262–274. https://doi.org/10.1038/nrm.2017.115.
4. El Khattabi, L., Zhao, H., Kalchschmidt, J., Young, N., Jung, S., Van Blerkom, P., Kieffer-Kwon, P., Kieffer-Kwon, K.R., Park, S., Wang, X., et al. (2019). A Pliable Mediator Acts as a Functional Rather Than an Architectural Bridge between Promoters and Enhancers. Cell *178*, 1145–1158.e20. https://doi.org/10.1016/j.cell.2019.07.011.
5. Adelman, K., and Lis, J.T. (2012). Promoter-proximal pausing of RNA polymerase II: emerging roles in metazoans. Nat. Rev. Genet. *13*, 720–731. https://doi.org/10.1038/nrg3293.
6. Core, L., and Adelman, K. (2019). Promoter-proximal pausing of RNA polymerase II: a nexus of gene regulation. Genes Dev. *33*, 960–982. https://doi.org/10.1101/gad.325142.119.
7. Conaway, R.C., and Conaway, J.W. (2013). The Mediator complex and transcription elongation. Biochim. Biophys. Acta *1829*, 69–75. https://doi.org/10.1016/j.bbagrm.2012.08.017.
8. Taatjes, D.J., Näär, A.M., Andel, F., 3rd, Nogales, E., and Tjian, R. (2002). Structure, function, and activator-induced conformations of the CRSP

coactivator. Science *295*, 1058–1062. https://doi.org/10.1126/science.1065249.

9. Knuesel, M.T., Meyer, K.D., Bernecky, C., and Taatjes, D.J. (2009). The human CDK8 subcomplex is a molecular switch that controls Mediator coactivator function. Genes Dev. *23*, 439–451. https://doi.org/10.1101/gad.1767009.

10. Li, T., Chao, T.C., and Tsai, K.L. (2024). Structures and compositional dynamics of Mediator in transcription regulation. Curr. Opin. Struct. Biol. *88*, 102892. https://doi.org/10.1016/j.sbi.2024.102892.

11. Tsai, K.L., Tomomori-Sato, C., Sato, S., Conaway, R.C., Conaway, J.W., and Asturias, F.J. (2014). Subunit Architecture and Functional Modular Rearrangements of the Transcriptional Mediator Complex. Cell *158*, 463. https://doi.org/10.1016/j.cell.2014.06.036.

12. Allen, B.L., and Taatjes, D.J. (2015). The Mediator complex: a central integrator of transcription. Nat. Rev. Mol. Cell Biol. *16*, 155–166. https://doi.org/10.1038/nrm3951.

13. Richter, W.F., Nayak, S., Iwasa, J., and Taatjes, D.J. (2022). The Mediator complex as a master regulator of transcription by RNA polymerase II. Nat. Rev. Mol. Cell Biol. *23*, 732–749. https://doi.org/10.1038/s41580-022-00498-3.

14. Takahashi, H., Parmely, T.J., Sato, S., Tomomori-Sato, C., Banks, C.A., Kong, S.E., Szutorisz, H., Swanson, S.K., Martin-Brown, S., Washburn, M.P., et al. (2011). Human mediator subunit MED26 functions as a docking site for transcription elongation factors. Cell *146*, 92–104. https://doi.org/10.1016/j.cell.2011.06.005.

15. Tsai, K.L., Sato, S., Tomomori-Sato, C., Conaway, R.C., Conaway, J.W., and Asturias, F.J. (2013). A conserved Mediator-CDK8 kinase module association regulates Mediator-RNA polymerase II interaction. Nat. Struct. Mol. Biol. *20*, 611–619. https://doi.org/10.1038/nsmb.2549.

16. Hengartner, C.J., Thompson, C.M., Zhang, J., Chao, D.M., Liao, S.M., Koleske, A.J., Okamura, S., and Young, R.A. (1995). Association of an activator with an RNA polymerase II holoenzyme. Genes Dev. *9*, 897–910. https://doi.org/10.1101/gad.9.8.897.

17. Firestein, R., Bass, A.J., Kim, S.Y., Dunn, I.F., Silver, S.J., Guney, I., Freed, E., Ligon, A.H., Vena, N., Ogino, S., et al. (2008). CDK8 is a colorectal cancer oncogene that regulates beta-catenin activity. Nature *455*, 547–551. https://doi.org/10.1038/nature07179.

18. Park, M.J., Shen, H., Spaeth, J.M., Tolvanen, J.H., Failor, C., Knudtson, J.F., McLaughlin, J., Halder, S.K., Yang, Q., Bulun, S.E., et al. (2018). Oncogenic exon 2 mutations in Mediator subunit MED12 disrupt allosteric activation of cyclin C-CDK8/19. J. Biol. Chem. *293*, 4870–4882. https://doi.org/10.1074/jbc.RA118.001725.

19. Klatt, F., Leitner, A., Kim, I.V., Ho-Xuan, H., Schneider, E.V., Langhammer, F., Weinmann, R., Müller, M.R., Huber, R., Meister, G., et al. (2020). A precisely positioned MED12 activation helix stimulates CDK8 kinase activity. Proc. Natl. Acad. Sci. USA *117*, 2894–2905. https://doi.org/10.1073/pnas.1917635117.

20. Daniels, D.L., Ford, M., Schwinn, M.K., Benink, H., Galbraith, M.D., Amunugama, R., Jones, R., Allen, D., Okazaki, N., Yamakawa, H., et al. (2013). Mutual Exclusivity of MED12/MED12L, MED13/13L, and CDK8/19 Paralogs Revealed within the CDK-Mediator Kinase Module. J. Proteomics Bioinform. *S2*, 004.

21. Elmlund, H., Baraznenok, V., Lindahl, M., Samuelsen, C.O., Koeck, P.J., Holmberg, S., Hebert, H., and Gustafsson, C.M. (2006). The cyclin-dependent kinase 8 module sterically blocks Mediator interactions with RNA polymerase II. Proc Natl Acad Sci USA *103*, 15788–15793. https://doi.org/10.1073/pnas.0607483103.

22. Donner, A.J., Ebmeier, C.C., Taatjes, D.J., and Espinosa, J.M. (2010). CDK8 is a positive regulator of transcriptional elongation within the serum response network. Nat. Struct. Mol. Biol. *17*, 194–201. https://doi.org/10.1038/nsmb.1752.

23. Nemet, J., Jelicic, B., Rubelj, I., and Sopta, M. (2014). The two faces of Cdk8, a positive/negative regulator of transcription. Biochimie *97*, 22–27. https://doi.org/10.1016/j.biochi.2013.10.004.

24. Galbraith, M.D., Allen, M.A., Bensard, C.L., Wang, X., Schwinn, M.K., Qin, B., Long, H.W., Daniels, D.L., Hahn, W.C., Dowell, R.D., et al. (2013). HIF1A employs CDK8-mediator to stimulate RNAPII elongation in response to hypoxia. Cell *153*, 1327–1339. https://doi.org/10.1016/j.cell.2013.04.048.

25. Abdella, R., Talyzina, A., Chen, S., Inouye, C.J., Tjian, R., and He, Y. (2021). Structure of the human Mediator-bound transcription preinitiation complex. Science *372*, 52–56. https://doi.org/10.1126/science.abg3074.

26. Zhao, H., Young, N., Kalchschmidt, J., Lieberman, J., El Khattabi, L., Casellas, R., and Asturias, F.J. (2021). Structure of mammalian Mediator complex reveals Tail module architecture and interaction with a conserved core. Nat. Commun. *12*, 1355. https://doi.org/10.1038/s41467-021-21601-w.

27. Chen, X., Yin, X., Li, J., Wu, Z., Qi, Y., Wang, X., Liu, W., and Xu, Y. (2021). Structures of the human Mediator and Mediator-bound preinitiation complex. Science *372*, eabg0635. https://doi.org/10.1126/science.abg0635.

28. Rengachari, S., Schilbach, S., Aibara, S., Dienemann, C., and Cramer, P. (2021). Structure of the human Mediator-RNA polymerase II pre-initiation complex. Nature *594*, 129–133. https://doi.org/10.1038/s41586-021-03555-7.

29. Tsai, K.L., Yu, X., Gopalan, S., Chao, T.C., Zhang, Y., Florens, L., Washburn, M.P., Murakami, K., Conaway, R.C., Conaway, J.W., et al. (2017). Mediator structure and rearrangements required for holoenzyme formation. Nature *544*, 196–201. https://doi.org/10.1038/nature21393.

30. Nozawa, K., Schneider, T.R., and Cramer, P. (2017). Core Mediator structure at 3.4 A extends model of transcription initiation complex. Nature *545*, 248–251. https://doi.org/10.1038/nature22328.

31. Gorbea Colón, J.J., Palao, L., 3rd, Chen, S.F., Kim, H.J., Snyder, L., Chang, Y.W., Tsai, K.L., and Murakami, K. (2023). Structural basis of a transcription pre-initiation complex on a divergent promoter. Mol. Cell *83*, 574–588.e11. https://doi.org/10.1016/j.molcel.2023.01.011.

32. Li, Y.C., Chao, T.C., Kim, H.J., Cholko, T., Chen, S.F., Li, G., Snyder, L., Nakanishi, K., Chang, C.E., Murakami, K., et al. (2021). Structure and non-canonical Cdk8 activation mechanism within an Argonaute-containing Mediator kinase module. Sci. Adv. *7*, eabd4484. https://doi.org/10.1126/sciadv.abd4484.

33. Yang, Z., Fang, J., Chittuluru, J., Asturias, F.J., and Penczek, P.A. (2012). Iterative stable alignment and clustering of 2D transmission electron microscope images. Structure *20*, 237–247. https://doi.org/10.1016/j.str.2011.12.007.

34. Schöenfeld, F., Stabrin, M., Shaikh, T.R., Wagner, T., and Raunser, S. (2022). Accelerated 2D Classification With ISAC Using GPUs. Front. Mol. Biosci. *9*, 919994. https://doi.org/10.3389/fmolb.2022.919994.

35. Zhong, E.D., Bepler, T., Berger, B., and Davis, J.H. (2021). CryoDRGN: reconstruction of heterogeneous cryo-EM structures using neural networks. Nat. Methods *18*, 176–185. https://doi.org/10.1038/s41592-020-01049-4.

36. Schneider, E.V., Böttcher, J., Blaesse, M., Neumann, L., Huber, R., and Maskos, K. (2011). The structure of CDK8/CycC implicates specificity in the CDK/cyclin family and reveals interaction with a deep pocket binder. J. Mol. Biol. *412*, 251–266. https://doi.org/10.1016/j.jmb.2011.07.020.

37. Jumper, J., Evans, R., Pritzel, A., Green, T., Figurnov, M., Ronneberger, O., Tunyasuvunakool, K., Bates, R., Žídek, A., Potapenko, A., et al. (2021). Highly accurate protein structure prediction with AlphaFold. Nature *596*, 583–589. https://doi.org/10.1038/s41586-021-03819-2.

38. Nakanishi, K., Weinberg, D.E., Bartel, D.P., and Patel, D.J. (2012). Structure of yeast Argonaute with guide RNA. Nature *486*, 368–374. https://doi.org/10.1038/nature11211.

39. Schirle, N.T., and MacRae, I.J. (2012). The crystal structure of human Argonaute2. Science *336*, 1037–1040. https://doi.org/10.1126/science.1221551.

40. Vulto-van Silfhout, A.T., de Vries, B.B., van Bon, B.W., Hoischen, A., Ruiterkamp-Versteeg, M., Gilissen, C., Gao, F., van Zwam, M., Harteveld, C.L., van Essen, A.J., et al. (2013). Mutations in MED12 cause X-linked Ohdo syndrome. Am. J. Hum. Genet. *92*, 401–406. https://doi.org/10.1016/j.ajhg.2013.01.007.

41. Kim, S., Xu, X., Hecht, A., and Boyer, T.G. (2006). Mediator is a transducer of Wnt/beta-catenin signaling. J. Biol. Chem. *281*, 14066–14075. https://doi.org/10.1074/jbc.M602696200.

42. Ding, N., Zhou, H., Esteve, P.O., Chin, H.G., Kim, S., Xu, X., Joseph, S.M., Friez, M.J., Schwartz, C.E., Pradhan, S., et al. (2008). Mediator links epigenetic silencing of neuronal gene expression with X-linked mental retardation. Mol. Cell *31*, 347–359. https://doi.org/10.1016/j.molcel.2008.05.023.

43. Erdős, G., Pajkos, M., and Dosztányi, Z. (2021). IUPred3: prediction of protein disorder enhanced with unambiguous experimental annotation and visualization of evolutionary conservation. Nucleic Acids Res. *49*, W297–W303. https://doi.org/10.1093/nar/gkab408.

44. Dimitrova, E., Feldmann, A., van der Weide, R.H., Flach, K.D., Lastuvkova, A., de Wit, E., and Klose, R.J. (2022). Distinct roles for CKM-Mediator in controlling Polycomb-dependent chromosomal interactions and priming genes for induction. Nat. Struct. Mol. Biol. *29*, 1000–1010. https://doi.org/10.1038/s41594-022-00840-5.

45. Robinson, P.J., Bushnell, D.A., Trnka, M.J., Burlingame, A.L., and Kornberg, R.D. (2012). Structure of the mediator head module bound to the carboxy-terminal domain of RNA polymerase II. Proc. Natl. Acad. Sci. USA *109*, 17931–17935. https://doi.org/10.1073/pnas.1215241109.

46. Schilbach, S., Wang, H., Dienemann, C., and Cramer, P. (2023). Yeast PIC-Mediator structure with RNA polymerase II C-terminal domain. Proc. Natl. Acad. Sci. USA *120*, e2220542120. https://doi.org/10.1073/pnas.2220542120.

47. Sato, S., Tomomori-Sato, C., Tsai, K.L., Yu, X., Sardiu, M., Saraf, A., Washburn, M.P., Florens, L., Asturias, F.J., Conaway, R.C., et al. (2016). Role for the MED21-MED7 Hinge in Assembly of the Mediator-RNA Polymerase II Holoenzyme. J. Biol. Chem. *291*, 26886–26898. https://doi.org/10.1074/jbc.M116.756098.

48. Milbradt, A.G., Kulkarni, M., Yi, T., Takeuchi, K., Sun, Z.Y.J., Luna, R.E., Selenko, P., Näär, A.M., and Wagner, G. (2011). Structure of the VP16 transactivator target in the Mediator. Nat. Struct. Mol. Biol. *18*, 410–415. https://doi.org/10.1038/nsmb.1999.

49. Vojnic, E., Mourão, A., Seizl, M., Simon, B., Wenzeck, L., Larivière, L., Baumli, S., Baumgart, K., Meisterernst, M., Sattler, M., et al. (2011). Structure and VP16 binding of the Mediator Med25 activator interaction domain. Nat. Struct. Mol. Biol. *18*, 404–409. https://doi.org/10.1038/nsmb.1997.

50. Grueter, C.E., van Rooij, E., Johnson, B.A., DeLeon, S.M., Sutherland, L.B., Qi, X., Gautron, L., Elmquist, J.K., Bassel-Duby, R., and Olson, E.N. (2012). A cardiac microRNA governs systemic energy homeostasis by regulation of MED13. Cell *149*, 671–683. https://doi.org/10.1016/j.cell.2012.03.029.

51. Li, T., Tang, H.C., and Tsai, K.L. (2023). Unveiling the noncanonical activation mechanism of CDKs: insights from recent structural studies. Front. Mol. Biosci. *10*, 1290631. https://doi.org/10.3389/fmolb.2023.1290631.

52. Liao, S.M., Zhang, J., Jeffery, D.A., Koleske, A.J., Thompson, C.M., Chao, D.M., Viljoen, M., van Vuuren, H.J., and Young, R.A. (1995). A kinase-cyclin pair in the RNA polymerase II holoenzyme. Nature *374*, 193–196. https://doi.org/10.1038/374193a0.

53. Cevher, M.A., Shi, Y., Li, D., Chait, B.T., Malik, S., and Roeder, R.G. (2014). Reconstitution of active human core Mediator complex reveals a critical role of the MED14 subunit. Nat. Struct. Mol. Biol. *21*, 1028–1034. https://doi.org/10.1038/nsmb.2914.

54. Davis, M.A., Larimore, E.A., Fissel, B.M., Swanger, J., Taatjes, D.J., and Clurman, B.E. (2013). The SCF-Fbw7 ubiquitin ligase degrades MED13 and MED13L and regulates CDK8 module association with Mediator. Genes Dev. *27*, 151–156. https://doi.org/10.1101/gad.207720.112.

55. Osman, S., Mohammad, E., Lidschreiber, M., Stuetzer, A., Bazsó, F.L., Maier, K.C., Urlaub, H., and Cramer, P. (2021). The Cdk8 kinase module regulates interaction of the mediator complex with RNA polymerase II. J. Biol. Chem. *296*, 100734. https://doi.org/10.1016/j.jbc.2021.100734.

56. Stieg, D.C., Willis, S.D., Ganesan, V., Ong, K.L., Scuorzo, J., Song, M., Grose, J., Strich, R., and Cooper, K.F. (2018). A complex molecular switch directs stress-induced cyclin C nuclear release through SCF(Grr1)-mediated degradation of Med13. Mol Biol Cell *29*, 363–375. https://doi.org/10.1091/mbc.E17-08-0493.

57. Clark, A.D., Oldenbroek, M., and Boyer, T.G. (2015). Mediator kinase module and human tumorigenesis. Crit. Rev. Biochem. Mol. Biol. *50*, 393–426. https://doi.org/10.3109/10409238.2015.1064854.

58. Xu, W., and Ji, J.Y. (2011). Dysregulation of CDK8 and Cyclin C in tumorigenesis. J. Genet. Genomics *38*, 439–452. https://doi.org/10.1016/j.jgg.2011.09.002.

59. Mäkinen, N., Mehine, M., Tolvanen, J., Kaasinen, E., Li, Y., Lehtonen, H.J., Gentile, M., Yan, J., Enge, M., Taipale, M., et al. (2011). MED12, the mediator complex subunit 12 gene, is mutated at high frequency in uterine leiomyomas. Science *334*, 252–255. https://doi.org/10.1126/science.1208930.

60. Turunen, M., Spaeth, J.M., Keskitalo, S., Park, M.J., Kivioja, T., Clark, A.D., Mäkinen, N., Gao, F., Palin, K., Nurkkala, H., et al. (2014). Uterine leiomyoma-linked MED12 mutations disrupt mediator-associated CDK activity. Cell Rep. *7*, 654–660. https://doi.org/10.1016/j.celrep.2014.03.047.

61. Park, M.J., Shen, H., Kim, N.H., Gao, F., Failor, C., Knudtson, J.F., McLaughlin, J., Halder, S.K., Heikkinen, T.A., Vahteristo, P., et al. (2018). Mediator Kinase Disruption in MED12-Mutant Uterine Fibroids From Hispanic Women of South Texas. J. Clin. Endocrinol. Metab. *103*, 4283–4292. https://doi.org/10.1210/jc.2018-00863.

62. Sun, P., Enslen, H., Myung, P.S., and Maurer, R.A. (1994). Differential activation of CREB by Ca2+/calmodulin-dependent protein kinases type II and type IV involves phosphorylation of a site that negatively regulates activity. Genes Dev. *8*, 2527–2539. https://doi.org/10.1101/gad.8.21.2527.

63. Budzyński, M.A., Puustinen, M.C., Joutsen, J., and Sistonen, L. (2015). Uncoupling Stress-Inducible Phosphorylation of Heat Shock Factor 1 from Its Activation. Mol. Cell. Biol. *35*, 2530–2540. https://doi.org/10.1128/MCB.00816-14.

64. Emsley, P., Lohkamp, B., Scott, W.G., and Cowtan, K. (2010). Features and development of Coot. Acta Crystallogr. D Biol. Crystallogr. *66*, 486–501. https://doi.org/10.1107/S0907444910007493.

65. Wagner, T., and Raunser, S. (2020). The evolution of SPHIRE-crYOLO particle picking and its application in automated cryo-EM processing workflows. Commun. Biol. *3*, 61. https://doi.org/10.1038/s42003-020-0790-y.

66. Punjani, A., Rubinstein, J.L., Fleet, D.J., and Brubaker, M.A. (2017). cryoSPARC: algorithms for rapid unsupervised cryo-EM structure determination. Nat. Methods *14*, 290–296. https://doi.org/10.1038/nmeth.4169.

67. Zheng, S.Q., Palovcak, E., Armache, J.P., Verba, K.A., Cheng, Y., and Agard, D.A. (2017). MotionCor2: anisotropic correction of beam-induced motion for improved cryo-electron microscopy. Nat. Methods *14*, 331–332. https://doi.org/10.1038/nmeth.4193.

68. Iacobucci, C., Götze, M., Ihling, C.H., Piotrowski, C., Arlt, C., Schäfer, M., Hage, C., Schmidt, R., and Sinz, A. (2018). A cross-linking/mass spectrometry workflow based on MS-cleavable cross-linkers and the MeroX software for studying protein structures and protein-protein interactions. Nat. Protoc. *13*, 2864–2889. https://doi.org/10.1038/s41596-018-0068-8.

69. Adams, P.D., Afonine, P.V., Bunkóczi, G., Chen, V.B., Davis, I.W., Echols, N., Headd, J.J., Hung, L.W., Kapral, G.J., Grosse-Kunstleve, R.W., et al. (2010). PHENIX: a comprehensive Python-based system for macromolecular structure solution. Acta Crystallogr. D Biol. Crystallogr. *66*, 213–221. https://doi.org/10.1107/S0907444909052925.

70. Scheres, S.H. (2012). RELION: implementation of a Bayesian approach to cryo-EM structure determination. J. Struct. Biol. *180*, 519–530. https://doi.org/10.1016/j.jsb.2012.09.006.

71. Sheng, Q., Li, R., Dai, J., Li, Q., Su, Z., Guo, Y., Li, C., Shyr, Y., and Zeng, R. (2015). Preprocessing significantly improves the peptide/protein identification sensitivity of high-resolution isobarically labeled tandem mass spectrometry data. Mol. Cell. Proteomics *14*, 405–417. https://doi.org/10.1074/mcp.O114.041376.

72. Pettersen, E.F., Goddard, T.D., Huang, C.C., Couch, G.S., Greenblatt, D.M., Meng, E.C., and Ferrin, T.E. (2004). UCSF Chimera–a visualization system for exploratory research and analysis. J. Comput. Chem. *25*, 1605–1612. https://doi.org/10.1002/jcc.20084.

73. Pettersen, E.F., Goddard, T.D., Huang, C.C., Meng, E.C., Couch, G.S., Croll, T.I., Morris, J.H., and Ferrin, T.E. (2021). UCSF ChimeraX: Structure visualization for researchers, educators, and developers. Protein Sci. *30*, 70–82. https://doi.org/10.1002/pro.3943.

74. Kosinski, J., von Appen, A., Ori, A., Karius, K., Müller, C.W., and Beck, M. (2015). Xlink Analyzer: software for analysis and visualization of cross-linking data in the context of three-dimensional structures. J. Struct. Biol. *189*, 177–183. https://doi.org/10.1016/j.jsb.2015.01.014.

75. Xu, A., Liu, M., Huang, M.F., Zhang, Y., Hu, R., Gingold, J.A., Liu, Y., Zhu, D., Chien, C.S., Wang, W.C., et al. (2023). Rewired m^6A epitranscriptomic networks link mutant p53 to neoplastic transformation. Nat. Commun. *14*, 1694. https://doi.org/10.1038/s41467-023-37398-9.

76. Tomomori-Sato, C., Sato, S., Conaway, R.C., and Conaway, J.W. (2013). Immunoaffinity purification of protein complexes from Mammalian cells. Methods Mol. Biol. *977*, 273–287. https://doi.org/10.1007/978-1-62703-284-1_22.

77. Zhang, K. (2016). Gctf: Real-time CTF determination and correction. J. Struct. Biol. *193*, 1–12. https://doi.org/10.1016/j.jsb.2015.11.003.

78. Henderson, R., Sali, A., Baker, M.L., Carragher, B., Devkota, B., Downing, K.H., Egelman, E.H., Feng, Z., Frank, J., Grigorieff, N., et al. (2012). Outcome of the first electron microscopy validation task force meeting. Structure *20*, 205–214. https://doi.org/10.1016/j.str.2011.12.014.

79. DeLano, W.L. (2002). The PyMOL Molecular Graphics System (Delano Scientific).

80. Shevchenko, A., Loboda, A., Ens, W., Schraven, B., Standing, K.G., and Shevchenko, A. (2001). Archived polyacrylamide gels as a resource for proteome characterization by mass spectrometry. Electrophoresis *22*, 1194–1203. https://doi.org/10.1002/1522-2683( )22:6<1194::AID-ELPS1194>3.0.CO;2-A.

Please cite this article in press as: Chao et al., Structural basis of the human transcriptional Mediator regulated by its dissociable kinase module, Molecular Cell (2024), https://doi.org/10.1016/j.molcel.2024.09.001

STAR★METHODS

KEY RESOURCES TABLE

REAGENT or RESOURCE	SOURCE	IDENTIFIER
Antibodies		
CDK8	Cell Signaling	Cat#4101; RRID:AB-1903934
FLAG	Sigma-Aldrich	Cat#F1804; RRID:AB_262044
GST	GenScript	Cat#A00865; RRID:AB_914654
MED6	Santa Cruz	Cat#sc-390474; RRID:AB_3073924
MED12	Cell Signaling	Cat#14360; RRID:AB_2798461
MED14	Bethyl Laboratories	Cat#A301-044A; RRID:AB_2266461
MED16	Bethyl Laboratories	Cat#A303-668A; RRID:AB_11205632
MED26	Cell Signaling	Cat#13641S; RRID:AB_2798281
MED29	Santa Cruz	Cat#sc-393800; RRID:AB_3661643
Protein A	Sigma-Aldrich	Cat#P1291; RRID:AB_1079562
RNA Pol II (8WG16)	Santa Cruz	Cat#sc-56767; RRID:AB_785522
RNA Pol II (Phospho S5)	Cell Signaling	Cat#13523; RRID:AB_2798246
Bacterial and virus strains		
DH10Bac Competent Cells	ThermoFisher	Cat#10361012
Rosetta(DE3) pLysS	Lab stock	N/A
E. coli BL21 DE3	Lab stock	N/A
Chemicals, peptides, and recombinant proteins		
3X (DYKDDDDK) Peptide	APExBIO	Cat#A6001
40% Acrylamide/Bis 19:1	Bio-Rad	Cat#1610144
Ampicillin	Sigma-Aldrich	Cat#A0166
ATP	Thermo Fisher Scientific	Cat#J10585-22
Ammonium Bicarbonate	Sigma Aldrich	Cat#09830-500G
NTP Set, 99% purity by HPLC, 100mM solutions of ATP, GTP, CTP and UTP	Thermo Fisher Scientific	Cat#R0481
Beta-mercaptoethanol	Sigma-Aldrich	Cat#63689
Creatine Kinase	Sigma Aldrich	Cat#10127566001
Cellfectin™ II Reagent	Thermo Fisher Scientific	Cat#10362100
DMEM	GenDEPOT	Cat#CM002-050
DTT	US Biological	Cat#D8070
Disuccinimidyl dibutyric urea crosslinker (DSBU)	Thermo Fisher Scientific	Cat#A35459
EDTA	Sigma Aldrich	Cat#EDS-500G
Ethanol	Decon Labs	Cat#2716
EX-CELL® 405 Serum-Free Medium for Insect Cells	MilliporeSigma	Cat#24405C
Formamide	Fisher Scientific Company	Cat#PI17899
Fetal bovine serum	Thermo Fisher Scientific	Cat#10438026
FreeStyle™ 293 Expression Medium	Thermo Fisher Scientific	Cat#12-338-018
Glycerol	Fisher BioReagents™	Cat#BP229-4
Glutathione	Sigma Aldrich	Cat#G4251-10MG
G418 Sulfate	Thermo Fisher Scientific	Cat#11811098
HEPES	Sigma-Aldrich	Cat#391338
Hygromycin B	Thermo Fisher Scientific	Cat#10687010
Iodoacetamide	Sigma-Aldrich	Cat#I6125-5G
Imidazole	Sigma-Aldrich	Cat#792527

(*Continued on next page*)

Please cite this article in press as: Chao et al., Structural basis of the human transcriptional Mediator regulated by its dissociable kinase module, Molecular Cell (2024), https://doi.org/10.1016/j.molcel.2024.09.001

Continued

REAGENT or RESOURCE	SOURCE	IDENTIFIER
Isopropyl b-D-1-thiogalactopyranoside, IPTG	Fisher Scientific	Cat#BP162010
Lipofectamine™ 3000 Transfection Reagent	Thermo Fisher Scientific	Cat#L3000015
LB Broth Miller	Fisher BioReagents™	Cat#BP1426-500
Magnesium dichloride, $MgCl_2$	Sigma-Aldrich	Cat#M8266
$Mg(SO_4)_2$	Boston BioProducts	Cat#MT-210
Mg(OAc)2	Sigma Aldrich	Cat#M5661-250G
NP-40	MilliporeSigma	Cat#492018
KOAc	Fisher Scientific Company	Cat#P171I-3
Phosphate Buffered Saline 10x solution	Fisher BioReagents™	Cat#BP399-1
PBS, pH 7.2	Thermo Fisher Scientific	Cat#20012027
Phosphocreatine pH 7.5	Sigma Aldrich	Cat#P7936-1G
Potassium chloride, KCl	Fisher BioReagents™	Cat#BP3661
Proteinase K	Sigma Aldrich	Cat#P4850
Protector RNase Inhibitor	Sigma-Aldrich	Cat#3335402001
Phenol:Chloroform:Isoamyl Alcohol 25:24:1 pH 8.0	Sigma-Aldrich	Cat#P3803-100ML
Pierce™ Trifluoroacetic Acid (TFA), LC-MS Grade	Thermo Fisher Scientific	Cat#85183
Pierce™ Water, LC-MS Grade	Thermo Fisher Scientific	Cat#85189
Precision Plus Protein Dual Color Standards	Bio-Rad	Cat#1610374
Reagent Alcohol, 70%	LabChem	Cat#LC222104
RNAse OUT	Thermo Fisher Scientific	Cat#10777019
Sodium chloride, NaCl	Fisher BioReagents™	Cat#BP358212
SDS	Sigma-Aldrich	Cat#L3771
SYBR Green PCR Master Mix	Bio-Rad	Cat#1725124
TRIzol reagent	Invitrogen	Cat#15596026
Triton X-100	Sigma-Aldrich	Cat#93443
Trypsin-EDTA (0.25%), phenol red	Thermo Fisher Scientific	Cat#25200056
Trypsin	Sigma-Aldrich	Cat#90057
Trichloroacetic acid (TCA)	VWR Life Science	Cat#BDH9310-500G
UTP [α-32P]	PerkinElmer	Cat#NEG507H250UC
Urea	Sigma-Aldrich	Cat#U5128-5KG
Uranyl Acetate	Ted Pella Inc.	Cat#19481
Critical commercial assays		
iScript cDNA synthesis kit	Bio-Rad	Cat#1708891
Deposited data		
Original gel, and western blot images for figures	This paper	Mendeley Data: https://doi.org/10.17632/2fr8m4sngm.1
XL-MS of the human CKM and cMED-CKM	This paper	ProteomeXchange: PXD044328
Cryo-EM map of the human CDK8 kinase module	This paper	EMDB: 41502
Cryo-EM map of the kinase lobe of human CDK8 kinase module	This paper	EMDB: 41499
Cryo-EM map of the kinase and central lobes of human CDK8 kinase module	This paper	EMDB: 41500
Cryo-EM map of the H-lobe of human MED12	This paper	EMDB: 41497
Cryo-EM map of the human transcriptional Mediator complex	This paper	EMDB: 41565
Cryo-EM map of the CKM-Hook of the human transcriptional Mediator complex	This paper	EMDB: 41509
Cryo-EM map of the Head-IDR of the human transcriptional Mediator complex	This paper	EMDB: 41511

(*Continued on next page*)

Please cite this article in press as: Chao et al., Structural basis of the human transcriptional Mediator regulated by its dissociable kinase module, Molecular Cell (2024), https://doi.org/10.1016/j.molcel.2024.09.001

Continued

REAGENT or RESOURCE	SOURCE	IDENTIFIER
Cryo-EM map of the Middle-IDR of the human transcriptional Mediator complex	This paper	EMDB: 41507
Cryo-EM map of the IDRc bound human core Mediator complex	This paper	EMDB: 41580
Cryo-EM map of the Head-IDRc of the human core Mediator complex	This paper	EMDB: 41512
Cryo-EM map of the Middle-IDRc of the human core Mediator complex	This paper	EMDB: 41513
Structure of the human CDK8 kinase module	This paper	PDB:8TQC
Structure of human transcriptional Mediator complex	This paper	PDB:8TQW
Structure of the IDRc bound human core Mediator complex	This paper	PDB:8TRH
Experimental models: Cell lines		
Human: Freestyle 293-F cells	Thermo Fisher Scientific	Cat#R79007
Human: 293T cells	ATCC	CRL3216
Human: U2OS cells	ATCC	HTB-96
Human: ES cells	WiCell	WA01
Trichoplusia ni: High Five cells	Thermo Fisher Scientific	Cat#B85502
Recombinant DNA		
Plasmid: pFastBac1-CDK8-Flag	Park et al.[18]	N/A
Plasmid: pFastBac1-CCNC-6xHis	Park et al.[18]	N/A
Plasmid: pFastBac1-MED12-HA	Park et al.[18]	N/A
Plasmid: pFastBac1-CBP-MED13	Park et al.[18]	N/A
Plasmid: pFastBac1-Flag-MED13	This paper	N/A
Plasmid: pFastBac1-Flag-MED13 (residues 1-1320)	This paper	N/A
Plasmid: pFastBac1-Flag-MED13 (residues 1070-2174)	This paper	N/A
Plasmid: pCDNA3.1-Hygro-Flag-CDK8	This paper	N/A
Plasmid: pCDNA3.1-Hygro-Flag-MED7	This paper	N/A
Plasmid: pCDNA3.1-Hygro-Flag-MED26	This paper	N/A
Plasmid: pCDNA3.1-Hygro-Flag-MED13	This paper	N/A
Plasmid: pCDNA3.1-Hygro-Flag-MED13	This paper	N/A
Plasmid: pCDNA3.1-Hygro-Flag-MED13-IDRc (residues 500-1069)	This paper	N/A
Plasmid: pCDNA3.1-Hygro-Flag-MED13 (Δ500-1069)	This paper	N/A
Plasmid: pCMV-Flag-MED13-IDRc	This paper	N/A
Plasmid: pCMV-Flag-MED13-IDRc (P929R/P930R)	This paper	N/A
Plasmid: pCMV-Flag-MED13-IDRc (P924R/S925R)	This paper	N/A
Plasmid: pCMV-Flag-MED13-IDRc (M916D/F917D/A918Y)	This paper	N/A
Plasmid: pSIN-Flag-MED13-IDRc	This paper	N/A
Plasmid: pGEX6P-1-GST-MED13 (residues 1-500)	This paper	N/A
Plasmid: pGEX6P-1-GST-MED13 (residues 500-1069)	This paper	N/A
Plasmid: pGEX6P-1-GST-MED13-IDRc (residues 500-750)	This paper	N/A
Plasmid: pGEX6P-1-GST-MED13 (residues 750-840)	This paper	N/A
Plasmid: pGEX6P-1-GST-MED13 (residues 840-1069)	This paper	N/A
Plasmid: pGEX6P-1-GST-MED13L-IDRc (residues 511-1107)	This paper	N/A
Plasmid: pGEX6P-1-GST-MED13-IDRc (F847D/S848Y/P849D)	This paper	N/A
Plasmid: pGEX6P-1-GST-MED13-IDRc (M916D/F917D/A918Y)	This paper	N/A
Plasmid: pGEX6P-1-GST-yMed13 (residues 1-312)	This paper	N/A
Plasmid: pGEX6P-1-GST-yMed13 (residues 313-562)	This paper	N/A
Plasmid: pGEX6P-1-GST-yMed13 (residues 563-700)	This paper	N/A
Plasmid: pGEX6P-1-GST-yMed13 (residues 701-813)	This paper	N/A

(*Continued on next page*)

Please cite this article in press as: Chao et al., Structural basis of the human transcriptional Mediator regulated by its dissociable kinase module, Molecular Cell (2024), https://doi.org/10.1016/j.molcel.2024.09.001

Continued

REAGENT or RESOURCE	SOURCE	IDENTIFIER
Plasmid: pGEX6P-1-GST-yMed13 (residues 814-1420)	This paper	N/A
Plasmid: pGEX6P-1-GST-yMed13 (residues 563-700)(VFA/DDK)	This paper	N/A
Plasmid: pGEX6P-1-GST-yMed13 (residues 563-700)(GGK/RRE)	This paper	N/A
Plasmid: pGEX6P-1-GST-VP16	This paper	N/A
Plasmid: pRL-TK	Promega	Cat#E2231
Plasmid: p5xGal4-TATA-luc	Sun et al.[62]	Addgene, Cat#46756
Plasmid: Gal4-VP16	Budzyński et al.[63]	Addgene, Cat#71728
Plasmid: Gal4-MED26	This paper	N/A
Oligonucleotides		
DNA primers utilized for qPCR analysis	This paper	Table S2
Software and algorithms		
Adobe Photoshop and Illustrator	Adobe	https://www.adobe.com/
AlphaFold	Jumper et al.[37]	https://alphafold.ebi.ac.uk/
Coot version 0.8.9.3	Emsley et al.[64]	https://www2.mrc-lmb.cam.ac.uk/personal/pemsley/coot/
crYOLO	Wagner et al.[65]	https://cryolo.readthedocs.io/en/stable/
cryoDRGN	Zhong et al.[35]	https://cryodrgn.cs.princeton.edu/
cryoSPARC version 3.1	Punjani et al.[66]	https://cryosparc.com/
Microsoft Office	Microsoft	https://www.microsoft.com/en-us/microsoft-365/microsoft-office
MotionCorr2	Zheng et al.[67]	https://emcore.ucsf.edu/ucsf-software
MeroX 2.0.0.5	Iacobucci et al.[68]	https://stavrox.com/
Phenix version 1.18.2	Adams et al.[69]	https://phenix-online.org/documentation/
PyMOL	Schrödinger and DeLano	https://pymol.org/2/
Relion version 3.1	Scheres[70]	https://www3.mrc-lmb.cam.ac.uk/relion/index.php/Main_Page
TurboRawToMGF 2.0.8	Sheng et al.[71]	https://github.com/shengqh/RCPA.Tools
Thermo Scientific™ Proteome Discoverer™ software version 1.4	Thermo Fisher Scientific	N/A
UCSF Chimera version 1.15	Pettersen et al.[72]	https://www.cgl.ucsf.edu/chimera/
UCSF ChimeraX version 1.6.1	Pettersen et al.[73]	https://www.cgl.ucsf.edu/chimerax/
Xlink Analyzer	Kosinski et al.[74]	https://www.embl-hamburg.de/XlinkAnalyzer/XlinkAnalyzer.html
Other		
ANTI-FLAG® M2 Affinity Gel	Sigma-Aldrich	Cat#A2220
Glutathione agarose beads	Cytiva	Cat#17513201
Beckman 45Ti rotor	Beckman Coulter Life Sciences	Cat#339160
Beckman SW60 Ti rotor	Beckman Coulter Life Sciences	Cat#335650
Sorvall ss-34 rotor	Thermo Fisher Scientific	Cat#28020TS

EXPERIMENTAL MODEL AND STUDY PARTICIPANT DETAILS

Freestyle 293-F cells (Flag-tagged CDK8, MED7, MED13 IDRc, and MED26) were maintained in FreeStyle™ 293 expression medium with 50 ug/ml G418 in shaking incubators at 37°C, humid atmosphere and 8% CO2. U2OS cells were maintained in DMEM medium supplemented with 10% (vol/vol) FBS at 37°C, humid atmosphere and 5% CO2. Human ES H1 cells (WA01) were cultured and expanded in mTeSR1 medium under feeder-free conditions. Sf9 insect cells were maintained in Sf-900TM II SFM (Gibco, Catalog #: 10902104) and High Five cells were maintained in Express Five™ SFM (Gibco, Catalog #: 10486025) with Antibiotic-

Antimycotic (Gibco, Catalog #: 15240062) in shaking incubators at 28°C. *E. coli* BL21(DE3) and Rosetta(DE3) pLysS cells which were used to express and purify all recombinant proteins were induced by addition of IPTG in LB medium.

METHOD DETAILS

Cell culture

The pcDNA3.1 plasmids encoding human Flag-tagged CDK8, MED13, MED7, and MED26 were generated and then transfected into Freestyle 293-F cells (293-F, ThermoFisher) using Lipofectamine 3000 (Invitrogen). Transfected cells were selected by treating 100 ug/ml G418 and maintained in FreeStyle™ 293 expression medium with 50 ug/ml G418. All 293-F cells were maintained in shaking incubators at 37°C, humid atmosphere and 8% CO_2 in a serum-free culture medium. U2OS cells were maintained in DMEM medium supplemented with 10% (vol/vol) FBS. Human ES H1 cells (WA01) were cultured and expanded in mTeSR1 medium under feeder-free conditions as previously described.[75]

Purification of human cMED-CKM and MED13 IDRc-bound cMED

For obtaining the cMED-CKM, 10 Liters of Freestyle 293 cells expressing CDK8-Flag were harvested, washed with cold 1x PBS twice, and resuspended in 250 ml hypotonic buffer (10 mM Hepes/KOH pH7.9, 1.5mM $MgCl_2$, 10 mM KCl, 0.5 mM Dithiothreitol, and protease inhibitors). After incubation on ice for 10 mins, the cells were homogenized in a Dounce homogenizer with 20 gentle strokes of the loose pestle. The cell lysate was centrifuged at 20,000 rpm for 30 mins at 4°C using a Beckman type 45Ti rotor, and the resulting pellet was washed by the hypotonic buffer twice, followed by centrifugation at 20,000 rpm for 10 mins at 4°C. Nuclear extract was prepared by following a protocol as described.[76] In brief, the pellet was gently suspended in 50 ml extraction buffer (25 mM Hepes/KOH pH7.9, 1.5mM $MgCl_2$, 0.3 M KCl, 0.5 mM DTT, 0.1 mM EDTA, 0.01% NP-40, 10% glycerol, and protease inhibitors) and rotated end-over-end for 1 hr at 4°C. The nuclear extract was centrifuged 33,000 rpm for 1 hr at 4°C in a Beckman type 45Ti rotor. The supernatant was collected and incubated with 4 ml anti-Flag M2 beads at 4°C for 4 hours with end-over-end rotation. The beads were loaded into a column and washed 4 times with 30 ml of washing buffer (25 mM Hepes/NaOH pH7.6, 1.5mM $MgCl_2$, 150 mM NaCl, 10% glycerol, 0.2 mM EDTA, 0.01% NP-40, and 2 mM beta-mercaptoethanol). The cMED-CKM complex was eluted with elution buffer (25 mM Hepes/NaOH pH7.6, 1.5mM $MgCl_2$, 150 mM NaCl, 10% glycerol, 0.2 mM EDTA, 0.01% NP-40, 2 mM beta-mercaptoethanol, and 200 ug/ml 1x FLAG peptide) at 4°C for 1 hr with end-over-end rotation. cMED-CKM eluted from anti-Flag M2 beads was concentrated and then loaded on a 15%-40% glycerol gradient (20 mM Hepes/NaOH pH7.6, 1 mM $MgCl_2$, 300 mM NaCl, 0.25 mM EDTA, and 1 mM beta-mercaptoethanol, and 15%-40% (v/v) glycerol), and centrifuged for 17 hours at 30,000 rpm using a Beckman SW60 Ti rotor. The fractions were examined by SDS-PAGE and western blotting. The peak fractions containing cMED-CKM complex were combined and dialyzed into buffer (20 mM Hepes/NaOH pH7.6, 1 mM $MgCl_2$, 300 mM NaCl, 0.25 mM EDTA, and 2.5 mM beta-mercaptoethanol). After dialysis, the cMED-CKM protein was examined by negative-stain EM, concentrated to ~1 mg/ml, and subjected to cryo-EM specimen preparation.

For the MED13 IDRc-bound cMED complex, 10 Liters of Freestyle 293 cells expressing Flag-tagged MED13 IDRc were harvested and subjected to protein purification following the procedure as described above. For structure determination, the purified IDRc-bound cMED complex was concentrated to ~2 mg/ml, and subjected to cryo-EM specimen preparation.

Expression and purification of recombinant human CKM

pFastBac1 plasmids encoding human CDK8-Flag, CCNC-6xHis, MED12-HA, and CBP-MED13 for baculovirus-based protein expression were generated and then transformed into DH10Bac competent cells (ThermoFisher) as previously described.[18] The bacmid DNAs isolated from white colonies were verified by DNA sequencing and used for transfection of Sf9 insect cells. After three rounds of viral amplification, four high-titer recombinant baculoviruses were used for co-infection of High Five cells (ThermoFisher). After 48 hours infection, 3 Liters of High Five cells were harvested and lysed with buffer A (20 mM Hepes/NaOH pH 7.9, 150 mM NaCl, 0.01% NP-40, 0.1mM EDTA, 10% glycerol, and protease inhibitors) using dounce homogenizer. Lysates were clarified by high-speed centrifugation (sorvall ss-34 rotor) at 18,000 rpm for 1 hour. The supernatant containing recombinant CKM proteins was incubated with anti-Flag M2 affinity beads for 1 hour at 4°C in buffer A. The CKM was washed four times, eluted with elution buffer (buffer A containing 200 ug/ml 1x FLAG peptide), and analyzed by SDS-PAGE. The CKM eluate was subjected to 15%-35% glycerol gradient centrifugation in buffer (20 mM Hepes/NaOH pH 7.9, 150 mM NaCl, 0.1mM EDTA, and 15%-35% (v/v) glycerol) with a SW60Ti rotor at 44,000 rpm for 16 hours at 4°C. The peak fractions containing CKM four subunits were pooled and concentrated, followed by buffer exchange into a buffer containing 20 mM Hepes/NaOH pH 7.9, 150 mM NaCl, and 0.1mM EDTA for subsequent kinase assay and structure determination.

Expression and purification of recombinant human MED13 proteins

DNA fragments encoding residues 1-500, 500-1069, 500-750, 750-840, 1-1320, 1070-2174, and 840-1069, as well as two IDRc mutants (M916D/F917D/A918Y and F847D/S848Y/P849D) of human MED13 were generated by PCR amplification using full-length MED13 DNA as a template. Except for the residues 1-1320 and 1070-2174, as well as two IDRc fragments (wild type and M916D/F917D/A918Y) of MED13 that were constructed into pFastBac1 for expression in insect cells, the remaining MED13 fragments were ligated into pGEX6P-1 for expression in *E.coli*. All constructs were verified by DNA sequencing. For GST pull-down

assays, each of the MED13 fragments, fused to the C terminus of GST protein, was expressed in *E. coli* Rosetta(DE3) pLysS cells followed by the procedure as described below.

GST pull-down assay

pGEX6P-1 plasmids encoding human CTD domain of Pol II RPB1 (residues 1593-1970) or MED13 fragments (residues 1-500, 500-1069, 500-750, 750-840, and 840-1069) were transformed into *E. coli* BL21(DE3) and Rosetta(DE3) pLysS cells, respectively. Protein expression was induced by addition of IPTG at a final concentration of 0.1 mM at 25°C for 5 hours. Cells were harvested and lysed by sonication. After centrifugation, the clarified lysate was incubated with 25 ul glutathione sepharose 4B beads (GE Healthcare) for 30 min at 4°C. The beads were washed three times using binding buffer (20 mM Hepes/NaOH pH 7.9, 300 mM NaCl, 0.01% NP-40, 10% glycerol, and protease inhibitors) followed by incubation at 4°C for 3 hours with 400 ul 293-F nuclear extracts or partially purified Mediator proteins that contain CKM- or Pol II-bound cMED, which were obtained using MED7-Flag following the same procedure as described above for CDK8-Flag. After binding, the beads were washed three times using binding buffer and then eluted using elution buffer containing 10 mM glutathione. The eluates were analyzed by SDS-PAGE and western blotting using anti-GST antibodies (GenScript, A00865), anti-MED14 antibodies (Bethyl Laboratories, A301-044A), anti-MED16 antibodies (Bethyl Laboratories, A303-668A), anti-MED6 antibodies (Santa Cruz, sc-390474), anti-MED26 antibodies (Cell Signaling, 13641S), and anti-Pol II CTD antibodies (8WG16). For yeast GST pull-down assay, purified GST, GST-VP16, and yeast GST-Med13-IDR(563-700) were immobilized on glutathione Sepharose 4B beads, followed by the addition of cell lysate from a FLAG-tagged Med7 yeast strain and incubation for 1 hour at 4°C. After four washes to remove unbound proteins, SDS-loading buffer was directly added to the beads for protein elution. The cMed, Pol II, and GST-fusion proteins were then detected by western blotting using the antibodies as indicated.

FLAG immunoprecipitation

To identify the cMED-binding region (MBR) on MED13, High Five cells for expressing full-length, or N-terminal (residues 1-1320) or C-terminal (residues 1070-2174) regions of Flag-tagged MED13 were prepared, harvest, and lysed following the same procedure as described above. After centrifugation, each supernatant was collected and incubated with 30 ul FLAG-M2 beads for 30 minutes at 4°C. After immobilization, the Flag beads were washed three times with binding buffer B (20 mM Hepes/NaOH pH7.9, 300 mM NaCl, 10% glycerol, 0.01% NP-40, 2 mM beta-mercaptoethanol) and then incubated with the 293-F nuclear extracts for 3 hours at 4°C. The beads were washed three times with binding buffer B and then eluted with the same buffer containing 200 ug/ml 1x FLAG peptide. To assess whether the interaction between cMED and CKM relies on the presence of MED13 IDRc, Freestyle 293 cells expressing Flag-tagged full-length MED13, MED13 with IDRc removed (ΔIDRc), or isolated MED13 IDRc were individually harvested and subsequently underwent protein purification following the aforementioned procedure. The eluates were analyzed by SDS-PAGE and western blotting using anti-FLAG M2 antibodies (Sigma-Aldrich, F1804), anti-MED14 antibodies (Bethyl Laboratories, A301-044A), anti-MED16 antibodies (Bethyl Laboratories, A303-668A), anti-MED6 antibodies (Santa Cruz, sc-390474), anti-MED12 antibodies (Cell Signaling, 14360) and anti-CDK8 antibodies (Cell Signaling, 4101).

Negative stain EM

3 μl of diluted cMED-CKM protein sample (~0.03 mg/mL) in buffer (20 mM Hepes/NaOH pH7.6, 200 mM NaCl, and 0.1 mM EDTA) was applied onto a carbon-coated and 300 mesh Cu/Rh grids (Ted Pella) following glow discharge treatment. After 1 min waiting, the excess of the sample was blotted using a piece of filter paper. Immediately after blotting, 3 μl of 2% uranyl acetate was applied onto the grid and then incubated for 1 min. The same blotting and staining steps were repeated twice. Then the grid was blotted dry from the edge with filter paper and allowed to dry. The stained grid was imaged on a JEOL 1400 electron microscope with a Rio9 camera (Gatan).

Cryo-EM specimen preparation, data collection, and image analysis

In brief, 3.0 μl of human CKM (~1 mg/ml) in buffer (25 mM Hepes/NaOH pH 7.9, 200 mM NaCl, and 0.1 mM EDTA) were directly applied onto freshly grow discharged 300 mesh C-flat™ holey carbon grids (CF-2/1-3C). Grids were blotted for 3–4 s at 4°C with 100% humidity and flash-frozen in liquid ethane using a Vitrobot mark IV (FEI). For cMED-CKM, 3.0 μl of concentrated protein (~0.5 mg/ml) in buffer (25 mM Hepes/NaOH pH 7.6, 150 mM NaCl, 0.1 mM EDTA, 2 mM $MgCl_2$, and 1 mM beta-mercaptoethanol) were applied onto grow discharged 300 mesh C-flat holey carbon grids. Frozen grids of cMED-MED13 IDRc (~2 mg/ml) were prepared using the same procedure as described above.

For cryo-EM data collection of CKM, the grids were imaged on a 300 kV Titan Krios electron microscope (FEI) using a GIF Quantum K2 direct electron detector (Gatan) operating in counting mode. Images were automatically collected at 0.6–3.0 um underfocus values with a nominal pixel size of 1.07 Å per pixel using EPU (Thermofisher). Each image was exposed for 8 s with a total dose of approximately 64 electrons per $Å^2$ which was fractioned into 40 frames. MotionCor2 was used to align frames.[67] The parameters of contrast transfer function (CTF) for each image were estimated using the program Gctf.[77] Initial particle picking by crYOLO[65] resulted in ~1.3 million particles. 2D clustering in cryoSPARC-2.5[66] was carried out to obtain a stack of ~30K images that was used to generate initial 3D models of CKM. 2D and 3D classification were carried out in RELION-3.1,[70] and identified a set of 107,310 images that were run through 3D refinement, Bayesian polishing, and CTF refinement to obtain a 3D map of overall CKM at an average

resolution of 3.8 Å, in which the secondary structures of the H-lobe were poorly defined due to mobility and conformational heterogeneity. For Kinase- and Kinase/Central-lobes of the CKM, the 107,310 images were further 3D classified and refined with a focused mask that covered corresponding regions, resulting in final maps at 3.8 and 3.6 Å resolution, respectively. For the H-lobe of CKM, we also started from the 107,310 images and performed 3D classification with a mask that only covered the H-lobe using RELION.[70] A final stack of 68,316 images were selected to run 3D refinement with the same mask, resulting in a final H-lobe map at 6.5 Å resolution. The resolutions of final 3D maps were estimated using gold standard Fourier Shell correlation (FSC) curves with 0.143 criteria.[78] RELION-3.1 or Cryosparc-2.5 were used to calculate local resolutions.

For cryo-EM data collection of the cMED-CKM, the grids were imaged on the same Titan Krios electron microscope equipped with a K2 direct electron detector with the following settings. Images were collected at 0.6-2.8 um underfocus values with a nominal pixel size of 1.42 Å per pixel using EPU counting mode. Each image was exposed for 12 s and fractioned into 48 frames with a total dose of approximately 52 electrons per $Å^2$. The movie frames were aligned by MotionCor2,[67] resulted in a total of 15,822 micrographs. crYOLO[65] was used for particle picking that resulted in a total of 467,838 particles. Multiple rounds of 2D classification in RELION/Cryosparc were performed to remove particles that lacked clear features, resulting in a stack of 290,607 particles. A subset of 25,316 particles was used for 3D initial model generation using Cryosparc. An initial model showing the CKM bound to cMED was low-pass filtered to 60 Å and used as a reference for carrying out 3D classification in RELION. This resulted in five classes with much better structural features than the others. These classes were combined into a stack of 105,401 images, which were subjected to 3D refinement that resulted in a 6.4 Å reconstruction. To obtain ISAC 2D averages, the 105,401 particles were converted to bdb format, followed by running GPU-ISAC in SPHIRE with default settings, including phase-flipping.[34] The resulting ISAC averages were further processed by Beautifier in SPHIRE, which performs local 2D alignment of ISAC2 2D clustering results using full CTF correction.[65] CTF refinement and Bayesian polishing were carried out to generate 105,401 shiny particles. 3D refinement of these shiny particles resulted in a 4.8 Å reconstruction, in which the CKM density was poor due to flexibility. Multiple runs of 3D classification were used to obtain a cMED-CKM class of 29,273 particles, which was subjected to 3D refinement that resulted in an average of 7.2 Å reconstruction (cMED-CKM). To visualize how CKM binds cMED, a loose mask covering the CKM and Hook was created and used to center the CKM-Hook of 105,401 shiny particles for subsequent multiple runs of local masked 3D classification. This resulted in a class in which CKM and the Hook of cMED were clearly visualized. 3D refinement of this class resulted in a 6.7 Å reconstruction (CKM-Hook). A mask that masked out the CKM and Hook was used to obtain a cMED-HookΔ map at an average resolution of 4.7 Å. For Head-IDR and Middle-IDR, two different loose masks that cover the Head and Middle, respectively, were created and used to center their corresponding regions of 105,401 shiny particles for performing focused 3D Classification following the similar procedures as described above. 3D refinement of Head-IDR and Middle-IDR classes resulted in two 4.9 Å reconstructions. The image analysis procedures and cryo-EM data collections of CKM and cMED-CKM are shown in Figure S2 and Table S1, respectively.

For cryo-EM data collection of the cMED-MED13 IDRc complex, the grids were prepared and imaged following the same settings of the CKM. Each image was exposed for 8 s with a total dose of approximately 56 electrons per $Å^2$, which was fractioned into 40 frames. In total, 7,608 movies were collected. The frame alignment, CTF estimation, and particle picking were following the same procedure as described above. A total of 239,553 particles were picked by crYOLO and subjected to multiple runs of RELION/Cryosparc 2D classification. After removing junk particles, a subset of ~50,000 particles from 195,612 particles was used for 3D initial model generation using Cryosparc. An initial model, which is similar to the cMED, was low-pass filtered to 60 Å and used as a reference for carrying out 3D classification in RELION. The selected classes, which show the intact cMED conformation, were combined and subjected to 3D refinement followed by CTF refinement and Bayesian polishing, resulting in an average 3.7 Å reconstruction. To perform local refinement, three masks were used to cover the Head module, Middle/MED14, and top portion of cMED, respectively. After multiple runs of 3D classification, 3D refinement of cMED-IDRc-Hinge and cMED-IDRc-Knob/MED6C, and cMED-IDRc-Neck classes resulted in 3.9 Å, 4.7 Å, and 4.2 Å reconstructions, respectively. The image analysis procedures and cryo-EM data collections of cMED-IDRc are shown in Figure S8 and Table S1, respectively.

To analyze the heterogeneity in the cryo-EM map of the Mediator complex caused by the presence of the flexible CKM, we employed the neural-network-based cryoDRGN version 2.3.[35] A total of 105,401 cMED-CKM particle images were processed, with alignment and CTF parameters derived from 3D refinements in RELION version 3.1. The particle stack had a pixel size of 1.40 Å per pixel and dimensions of 352 x 352 pixels. The encoder model comprised 3 layers with a width of 1024, while the decoder model included 3 layers with a width of 2048. The real-space windowing radius was set to 0.90 of the particle image. All other settings adhered to the defaults of cryoDRGN version 2.3. To analyze the heterogeneity in the cryo-EM map of the cMED-MED13 IDRc complex, the cryoDRGN was used following the same procedure as described above.

Model building and refinement

To build an atomic model of the CKM, we used the x-ray structure of human CDK8/CCNC [PDB: 3RGF] and AlphaFold models of human MED12 and MED13 as templates, which were fitted into the cryo-EM maps of the CKM by rigid-body fitting using Chimera.[72] After fitting, some regions of the templates, such as MED12N, MED12C, MED13 IDR, and flexible loops/coils that showed different conformations from the cryo-EM maps or had no density were removed from the model. The regions of the MED12N and MED12C were of sufficient quality for *ab initio* model building. The model building and adjustments were done using Coot.[64] Model refinement

Please cite this article in press as: Chao et al., Structural basis of the human transcriptional Mediator regulated by its dissociable kinase module, Molecular Cell (2024), https://doi.org/10.1016/j.molcel.2024.09.001

of the Kinase-lobe, Kinase/Central-lobes. and H-lobe against their corresponding cryo-EM maps were done by using the real-space refinement in Phenix.[69] These models were fitted into the overall map of CKM and then combined as the final overall structure.

Model building for cMED-CKM was facilitated by using our CKM model and published cryo-EM structure of human cMED [PDB: 7EMF] in which we removed MED26 due to its absence in our cMED-CKM specimen. These two structures were firstly fitted into the overall cryo-EM map of cMED-CKM using Chimera, resulting in an overall model of the cMED-CKM complex. The model of CKM with the Hook of MED, including MED10, MED19, and the N terminus of MED14, from the overall model was then fitted into the cryo-EM map of CKM-Hook, manually adjusted using Coot, and refined by real-space refinement in Phenix. The cMED structure without the Hook was divided into Head, Middle, and Tail portions, and individually fitted into the cryo-EM map of the cMED-HookΔ map by rigid-body fitting using Chimera. The fitted cMED model was manually adjusted and refined using the same procedure as described above. Both refined models of CKM-Hook and cMED without Hook were combined to generate an overall structure of cMED-CKM.

Model building for cMED-MED13 IDRc was aided by utilizing the published cryo-EM structure of human cMED [PDB: 7EMF]. Following the placement of the structure (with MED26 removed) into the cryo-EM density map through rigid-body fitting using Chimera,[72] extra densities were identified at the Neck domain of the Head module, the interface between MED6 C-terminal helix (H6) and MED14, as well as the MED21/7 Hinge of the Middle module. The density at the MED21/7 Hinge of the Middle module was used for *ab initio* model building. The fitted cMED-MED13 IDRc model was manually adjusted and refined using the same procedure as described above. The final overall models of CKM, cMED-CKM, and cMED-MED13 IDRc were validated using MolProbity (Table S1).[69] Phenix was used to calculate real-space map-model difference maps. All molecular graphic figures, including overall and local density maps, were made by Chimera, UCSF Chimera X,[73] or PyMOL.[79]

In vitro kinase assay

A GST-CTD-6xHis plasmid that contains the CTD domain of human Pol II RPB1 (residues 1593-1970) with a 6xHis-tag at its C-terminus was expressed in *E. coli* and purified using glutathione Sepharose 4B beads (GE Healthcare). Purified CKM (3 μM) or cMED-CKM (3 μM) was incubated at 30°C for 30 min in a kinase reaction buffer (100 μL), containing 1x PBS (pH 7.4), 10 mM $MgCl_2$, 1 mM ATP, and purified GST-CTD-6xHis substrate. Reactions were terminated by adding 20 μL 6xSDS sample buffer. Samples were resolved on 10% SDS-PAGE and analyzed by western blot using anti-Pol II-CTD antibody (8WG16) and monoclonal anti-FLAG M2 antibody (MilliporeSigma, F1804). The antibody (Cell Signaling, 13523) that recognizes phosphorylated Ser5 of CTD was used to detect CTD phosphorylation.

XL-MS analyses of the CKM and cMED-CKM

The recombinant human CKM purified by anti-Flag M2 affinity beads and glycerol gradient centrifugation was dialyzed into buffer (20 mM Hepes/NaOH pH 7.9, 150 mM NaCl, and 0.1mM EDTA) and concentrated to ~1 mg/ml. Around 100 ug CKM protein was incubated with disuccinimidyl dibutyric urea crosslinker (DSBU) at a final concentration of 6 mM for 2 hours on ice. The reaction was quenched with Ammonium Bicarbonate and further incubated for 30 min on ice. Crosslinked proteins were subjected to TCA precipitation. For cMED-CKM, proteins eluted from anti-Flag M2 beads were dialyzed into buffer (20 mM Hepes/NaOH pH7.6, 1 mM $MgCl_2$, 200 mM NaCl, 0.25 mM EDTA, and 1 mM beta-mercaptoethanol) and concentrated to ~1.5 mg/ml. Around 200 ug cMED-CKM protein was crosslinked, quenched, and precipitated following the same procedures applied to CKM.

Crosslinked proteins were reduced with 10 mM DTT for 30 min at 30°C, followed by alkylation with iodoacetamide (50 mM final, Sigma Aldrich) for 30 min at 30°C. The proteins were processed by S-TrapTM (Protifi) with its recommended protocol: with trypsin in 1:10 (w/w) enzyme-to- protein ratio for an hour at 30°C. Eluted peptides were dried under vacuum and resuspended with the peptide fractionation elution buffer: LC-MS grade 70% (v/v) water, 30% (v/v) Acetonitrile (ACN), and 0.1% (v/v) Trifluoroacetic acid (TFA). Peptide fraction was performed on AKTA pure 25 with Superdex 30 Increase 3.2/300 (GE Healthcare) at a flow rate of 30 μl min-1 of the elution buffer with a 100 μl fraction volume. Fractions containing enriched crosslinked peptides, which were empirically determined by the elution profile, retained and dried under vacuum, and resuspended with 0.1% (v/v) TFA containing LC-MS grade water for mass spectrometry analysis. Each fraction was analyzed on a Q-Exactive HF mass spectrometer (Thermo Fisher Scientific) coupled with Dionex Ultimate 3000 UHPLC system (Thermo Fischer Scientific) with in-house C18 column. Half of each sample amount was injected for the analysis and separated on 90-min gradient: mobile phase A (99.9% water with 0.1% formic acid (Sigma Aldrich); mobile phase B (80% ACN with 0.1% formic acid); starting 5% B, increased to 45% B for 90 min, then keep B constant at 90% for 5 min, and sharply decreased to 5% B for 5 min for re-equilibration of the column with the constant flow rate set to 400 nl min-1. The data dependent acquisition method was set as follows: Full MS resolution 120,000; MS1 AGC target 1e6; MS1 Maximum IT 200ms; Scan range 300 to 1800; dd-MS/MS resolution 30,000; MS/MS AGC target 2e5; MS2 Maximum IT 300ms; Fragmentation was enforced by higher-energy collisional dissociation with stepped collision energy with 25, 27, 30; Loop count Top 12;Isolation window 1.5; Fixed first mass 130; MS2 Minimum AGC target 800; Charge exclusion: unassigned,1,2,3,8,>8; Peptide match off; Exclude isotope on; Dynamic exclusion 45sec. Raw files were converted to mgf format with TurboRawToMGF 2.0.8[71]: Precursor mass weight range 300 – 10,000 Da and all default removal options were off. Searches for crosslinked peptides were performed by MeroX 2.0.1.4[68] with the default setting for DSBU with the minor modifications: Mass limit from 300 Da to 10,000 Da, Minimum charge (MS1) set to 4, Apply Prescore and Score cut off to 10, and FDR cut off set to 1%. All search results from each fraction's MS acquisition was combined and filtered by recalculated FDR at 1%. Redundant crosslinked pairs were sorted by the main score and the top hit was chosen for the final report table and mapping onto the structure in Chimera[72] with Xlink Analyzer plugin.[74]

Please cite this article in press as: Chao et al., Structural basis of the human transcriptional Mediator regulated by its dissociable kinase module, Molecular Cell (2024), https://doi.org/10.1016/j.molcel.2024.09.001

LC-MS-MS analyses of purified Mediator proteins

2 L of 293-F cells expressing Flag-tagged CDK8, MED13 IDRc, or MED26 was used to prepare nuclear extract following the same procedure as described above. Proteins purified from nuclear extract using anti-Flag M2 beads were applied to 15%-40% glycerol gradient centrifugation following the sample protocols as described above. The peak fractions containing large Mediator complexes were merged and dialyzed into buffer (20 mM Hepes/NaOH pH7.6, 1 mM $MgCl_2$, 150 mM NaCl, 1 mM EDTA, 1 mM beta-mercaptoethanol, and 5% glycerol). The protein samples were concentrated and processed by SDS-PAGE. The gel band samples were subjected to In-gel digestion.[80]

An aliquot of the tryptic digest (in 2 % acetonitrile/0.1% formic acid in water) was analyzed by LC/MS/MS on an Orbitrap FusionTM TribridTM mass spectrometer (Thermo ScientificTM) interfaced with a Dionex UltiMate 3000 Binary RSLCnano System. Peptides were separated onto an analytical C18 column (100μm ID x 25 cm, 5 μm, 18Å) at flow rate of 350 nl/min. Gradient conditions were: 3%-22% B for 40 min; 22%-35% B for 10min; 35%-90% B for 10 min; 90% B held for 10 min (solvent A, 0.1 % formic acid in water; solvent B, 0.1% formic acid in acetonitrile). The peptides were analyzed using data-dependent acquisition method, Orbitrap Fusion was operated with measurement of FTMS1 at resolutions 120,000 FWHM, scan range 350-1500 m/z, AGC target 2E5, and maximum injection time of 50 ms; During a maximum 3 second cycle time, the ITMS2 spectra were collected at rapid scan rate mode, with HCD NCE 34, 1.6 m/z isolation window, AGC target 1E4, maximum injection time of 35 ms, and dynamic exclusion was employed for 20 seconds. The raw data files were processed using Thermo ScientificTM Proteome DiscovererTM software version 1.4, spectra were searched against the Uniprot-Homo sapiens database using Sequest. Search results were trimmed to 1% FDR for strict and 5% for relaxed condition using Percolator. For the trypsin, up to two missed cleavages were allowed. MS tolerance was set 10 ppm; MS/MS tolerance 0.8 Da. Carbamidomethylation on cysteine residues was used as fixed modification; oxidation of methione as well as phosphorylation of serine, threonine, and tyrosine was set as variable modifications.

Competitive binding assays

To examine the impact of MED13 IDRc on the interaction between Pol II CTD and cMED (Figure 5I), 5 μg of purified GST-tagged Pol II-CTD was incubated with 30 μl of glutathione sepharose 4B beads (GE Healthcare) in buffer A (20 mM Hepes/NaOH pH 7.9, 300 mM NaCl, 0.01% NP-40, 10% glycerol, and protease inhibitors) for 1 hour at 4 °C. Subsequently, the beads underwent three washes using buffer A. Purified cMED proteins obtained via Flag-tagged MED7 from HEK293 cells were then introduced, and the mixture was incubated for 1 hour at 4 °C. Following three additional washes with buffer A, varying concentrations (0.2 μM, 0.5 μM, and 1.0 μM) of purified EGFP or EGFP-IDRc were added, and the mixture was further incubated for 1 hour at 4 °C. Following incubation, the beads were washed three times with the buffer A and then eluted with buffer A containing 10 mM glutathione. The eluted samples were subsequently subjected to analysis by western blotting. To assay the effects of human IDRc mutants on Pol II CTD-cMED interaction (Figure 5L), purified cMED proteins were combined with distinct concentrations (0.1μM and 1.0μM) of purified Flag-tagged wild-type MED13 IDRc or Mut2 (M916D/F917D/A918Y). The resulting mixtures were subsequently incubated with 30 μl GST-Pol II CTD-immobilized glutathione sepharose 4B beads (GE Healthcare) in buffer A for 2 h at 4 °C. Beads were washed three times using the buffer A. Bound proteins were then eluted using elution buffer containing 10 mM glutathione and analyzed by western blotting. For the reverse experiment (Figure 5K), 5 μg of purified Flag-tagged MED13 IDRc was incubated with 30 μl of anti-Flag M2 agarose resin in buffer A for 1 h at 4 °C. Following this, the resin was subjected to three washes using buffer A. Subsequently, 293-F nuclear extracts were added, and the mixture was incubated for 1 hour at 4 °C. After three additional washes with buffer A, varying concentrations (0.2 μM, 0.5 μM, and 1.0 μM) of either GST or GST-CTD were introduced into the mixture and incubated for 1 hour at 4 °C. The beads were washed three times with binding buffer A and then eluted with 200 ug/ml 1x Flag peptide. The eluates were analyzed by western blotting. To assay the effect of IDRc on MED26-cMED interaction (Figure 5J), 5 μg of purified Flag-tagged MED26 was incubated with 30 μl of anti-Flag M2 agarose resin in buffer A for 1 h at 4 °C. Following this, the resin was subjected to three washes using buffer A. Subsequently, 293-F nuclear extracts were added, and the mixture was incubated for 1 hour at 4 °C. After three additional washes with Buffer A, varying concentrations (0.2 μM, 0.5 μM, and 1.0 μM) of either EGFP or EGFP-IDRc were introduced into the mixture and incubated for 1 hour at 4 °C. The beads were washed three times with binding buffer A and then eluted with 200 ug/ml 1x Flag peptide. The eluates were analyzed by western blotting using anti-GST antibodies (GenScript, A00865), anti-Flag M2 antibodies (Sigma- Aldrich, F1804), anti-MED16 antibodies (Bethyl Laboratories, A303-668A), and anti-MED6 antibodies (Santa Cruz, sc-390474).

For the yeast competition assay, 5 μg of purified GST-tagged yeast Pol II-CTD protein was incubated with 30 μl of glutathione resin for 1 h at 4 °C. The resins were then washed four times with the buffer B (20 mM Hepes/NaOH pH 7.9, 200 mM NaCl, 0.02% NP-40, 10% glycerol, and 1 mM beta-mercaptoethanol) with protease inhibitors. Next, yeast whole cell extract containing FLAG-tagged Med7 and Protein A-tagged Med22 was added, and the mixture was incubated for 1 h at 4 °C. After four times of washes with the Buffer B, distinct concentrations (0.1μM and 1.0μM) of purified recombinant Flag-tagged wild-type Med13 IDR (563-813) or mutants (VFA/DDK and GGK/RRE), was added, and the mixture was incubated for 1 h at 4 °C. After four times of washes with the buffer B, the proteins were eluted with SDS-PAGE sample buffer and examined by western blotting using the antibodies as indicated.

Mapping of cMed interaction region on yeast Med13

The GST-tagged yMed13 fragments, including residues 1–312, 313–562, 563–700, 701–813, and 813–1420, were expressed in E. coli Rosetta (DE3). Each expressed protein was incubated with 30 μl of Glutathione beads for 1 h at 4 °C. The beads were then washed three times with Washing Buffer C (25 mM HEPES/NaOH pH7.6, 200 mM NaCl, 10% glycerol, 0.5 mM EDTA, 2 mM

Please cite this article in press as: Chao et al., Structural basis of the human transcriptional Mediator regulated by its dissociable kinase module, Molecular Cell (2024), https://doi.org/10.1016/j.molcel.2024.09.001

MgCl2, 2.5mM β-ME, and 0.05% NP-40). Next, yeast whole cell extract containing cMed with FLAG-tagged Med7 and Protein A-tagged Med22 was added to the beads and incubated for 1 h at 4 °C. Subsequently, the beads were washed three times with the same washing buffer. The bound proteins were eluted with SDS–PAGE sample buffer and subjected to western blot analysis using mouse anti-GST monoclonal antibody (A00865, GeneScript; 1:1,000) and mouse anti-FLAG monoclonal antibody (F1804, Sigma-Aldrich; 1:1,000) to detect yMed13 variants and cMED, respectively.

GST-tagged wild-type yeast Med13 IDR(563-700) and its mutants (VFA/DDK and GGK/RRE) expressed in and purified from E. coli. Purified proteins were immobilized on Glutathione beads for 1 h at 4 °C followed by four times of wash using binding buffer. Next, yeast whole cell extract containing cMed proteins with FLAG-tagged Med7 was added to the beads and incubated for 1 h at 4 °C. After four washes to remove unbound proteins, SDS-PAGE sample buffer was directly added to the beads. The amount of cMED bound to GST-yMed13-IDR wild-type and mutant variants was then analyzed by western blotting using mouse anti-FLAG antibody (F1804, Sigma-Aldrich; 1:1,000).

Luciferase reporter assays

HEK293 cells were transfected using Lipofectamine 3000 (Invitrogen) with the following plasmids as described in the text: p5xGal4-TATA-luc, pRL-TK-luc, pCMV, pGal4-MED26, pGal4-VP16, and pCMV-MED13, IDRc, and its mutants. After 24 h of transfection, cells were harvested, and luciferase activity was determined using the Dual-Glow System (Promega).

RT-qPCR

Flag-tagged MED13 IDRc and control lentiviruses were produced by packaging them in the HEK293T cell line using psin-MED13 IDRc and psin-vector plasmids, along with pMD2.G and psPAX2 plasmids. The lentiviruses were collected 48 hours after transfection and freshly added to human U2OS and ES cell lines. Subsequently, the cells were collected 60 hours after virus transduction and subjected to RT-qPCR analysis. RT-qPCR was performed as described.[75] Total RNA was extracted using TRIzol reagent (Invitrogen, 15596026) according to the manufacturer's protocol. Then 1 μg RNA was used for reverse transcription using the iScript cDNA synthesis kit (Bio-Rad Laboratories, 1708891). Quantitative Real-time PCR was conducted at a CFX96 machine (Bio-Rad Laboratories). A total of 20 μl qPCR reaction solution includes 10 μl SYBR Green PCR Master Mix (Bio-Rad Laboratories, 1725124), 1 μl cDNA, 1 μl 10 μM forward primer, 1 μl 10 μM reverse primer, and 7 μl molecular grade water. The GAPDH gene was used as a housekeeping control. Primer sequences are listed in Table S2.

Yeast transcription assay

The *in vitro* transcription assays were performed as previously described.[31] Reactions were performed with 0.25 pmol of 306-bp Gal4-SNR20 promoter DNA template, 0.5 pmol of 204-bp HIS4 promoter DNA fragment (competitor DNA), 300 μg of yeast whole cell extract, and 3 pmol of TBP were mixed and incubated with or without 5 pmol of Gal4-VP16 in the presence or absence of different amounts of purified CKM or wild-type Med13 IDR and its mutants. CKM was purified through affinity purification using a TAP tag on CycC as previously described.[32] In brief, the reaction was diluted with Buffer 100 (30 mM Hepes/KOH pH 7.6, 5% Glycerol, 5 mM DTT, 100 mM KOAc, 3.5 mM Mg(SO4)2) to 16 uL followed by incubation for 90 minutes at room temperature. Next, equal volume of radioactive 2X NTP Mix (80 mM Hepes/KOH, pH 7.6, 10 mM MgOAc, 2 mM ATP, 2 mM CTP, 2 mM GTP, 0.2 mM UTP, 82.5 nM P32-alpha-UTP, 80 mM Phosphocreatine pH 7.5, 30 ug Creatine Kinase, 12 U RNAse Out, 5 mM DTT), was added to the reaction to begin transcription. Transcription reaction was stopped in 10 min by adding 200 uL of Stop Buffer 1 (10 mM Tris-HCl, 300 mM NaCl, 5 mM EDTA, 300 U RNAse T1) followed by incubation at 37 °C for 15 min. Subsequently, Stop Buffer 2 (9.6% SDS, 5 ug Proteinase K) were added, and the solution was incubated at 37 °C for 30 min. Next, phenol-chloroform extraction was performed. The sample was stored at -20 °C overnight. Precipitated nucleic acids were pelleted by centrifugation. Next, the supernatant was pipetted off, and the sample was placed in a heating block at 40 °C to evaporate the rest of the EtOH. Finally, the pellet was resuspended with 12 μL of formamide dye and run on a denaturing Urea-PAGE (7 M Urea 6% Acrylamide gel). Gels were exposed to PhosphorImager screens at -20 °C overnight before imaging.

QUANTIFICATION AND STATISTICAL ANALYSIS

Overall and local resolution values for cryo-EM maps (Figures S2 and S6) were calculated using Relion, based on the gold-standard Fourier Shell Correlation (GFSC) method with a 0.143 criterion. Refinement statistics in the Table S1 for atomic coordinates were calculated using Phenix. Biological replicates are noted in the relevant legends.